arXiv:2606.08104v1 [cs.RO] 6 Jun 2026

Reinforcement learning in linear embedding space unlocks generalizable control across soft robot configurations

Xinglong Zhang[1*†], Cong Li[1†], Hangjie Mo[2†], Yue Jiang[1], Wenyu Cao[1], Xin Xu[1*], Wei Jiang[1], Zhenshan Bing[3,4], Yihe Yang[1], Xiaojian Li[2], Yueneng Yang[5], Huimin Lu[1], Ling-li Zeng[1], Alois Knoll[4], Dewen Hu[1*], Li Wen[6], Wei Pan[7]

[1*]College of Intelligence Science and Technology, National University of Defense Technology, Deya Road, Changsha, 410003, Hunan, China.

[2] School of Management, Hefei University of Technology, Nanyihuan Road, Hefei, 230002, Anhui, China.

[3]State Key Laboratory for Novel Software Technology and the School of Science and Technology, Nanjing University (Suzhou Campus), Taihu Road, Suzhou, 215163, China.

[4]School of Computation, Information and Technology, Technical University of Munich, Boltzmann Strasse, Munich, 85748, Germany.

[5]College of Aerospace Science and Engineering, National University of Defense Technology, Deya Road, Changsha, 410003, Hunan, China.

[6]School of Mechanical Engineering and Automation, Beihang University, Changping, Beijing, 100191, China.

[7]School of Engineering, Newcastle University, Claremont Road, Newcastle-upon-Tyne, NE1 7RU, UK.

[†]These authors contributed equally to this work.

Abstract

Soft-bodied organisms such as octopuses and elephant trunks exhibit remarkable morphological adaptability, dynamically reconfiguring body shape and stiffness, and flexibly adjusting their control strategies to enable versatile behaviors[1, 2]. Inspired by these biological systems, various soft robots have emerged in recent decades, featuring diverse materials, stiffnesses, and morphologies tailored to specific tasks. Despite substantial advances in the materials and structural designs of soft robots[3–5], developing a generalizable control framework capable of rapid adaptation across diverse configurations remains a long-standing challenge. Existing controllers are limited to fixed configurations, demanding laborious configuration-specific remodelling and policy redesign for new configurations[6–8]. Here, we introduce a generalizable control system that enables rapid adaptation across diverse soft robot configurations via reinforcement learning in a shared linear Koopman embedding space. By encoding robot dynamics into this embedding space, our method decouples control policies from specific morphologies, allowing real-time, model-free policy adaptation across diverse configurations without retraining from scratch. We validate our system across 30 soft robot configurations with different materials, stiffnesses, structural geometries, and assembly patterns, achieving substantial performance gains, including a 75× reduction in training samples compared to state-of-the-art methods, while sustaining robust performance under high-speed (1.89 $m \cdot s^{-1}$), high-payload (1 kg) and multiactuator faults. Our system enables a single base policy, with online updates, to achieve a wide range of real-world skills previously unattainable in soft robotics, such as forceful nail hammering, delicate

drinks serving, fluid calligraphy brush handwriting, and quick hand-eye reaction games. This work establishes a unified and adaptable control paradigm for diverse soft robot configurations, bridging mechanical reconfigurability with control flexibility, and may offer broader insights for generalizable control in complex physical systems.

Natural soft-bodied organisms demonstrate remarkable morphological adaptability through dynamic reconfiguration and adaptive control[1, 2, 9, 10]. For instance, octopuses reshape their body structures and elephant trunks modulate stiffness to enable versatile functionality that ranges from agile locomotion to flexible manipulation. This adaptability stems from embedded sensorimotor loops that continuously adjust to structural changes, allowing seamless multitask execution. Inspired by biological systems, soft robots leverage compliant materials and structures to achieve inherent adaptability and safe interaction[3, 11–14]. These features enable applications in delicate manipulation[11], human-robot cooperation[4], and confined-space navigation[15]. Despite advances in material design and structural reconfiguration of soft robots to meet diverse task demands[5, 16, 17], developing a generalizable control framework capable of fast adaptation across diverse configurations remains a long-standing problem[16, 18]. Existing controllers are typically configuration-specific, requiring extensive remodelling or controller redesign for each configuration[6–8, 19], limiting the scalable deployment of soft robots.

One challenge for multi-configuration adaptation is the domain expertise and intensive labor required for dynamical modelling of soft robots[20]. Analytical modelling methods, such as the Cosserat rod theory, achieve high modelling accuracy under quasi-static conditions for specific configurations but come with prohibitive computational costs[21, 22]. Data-driven modelling approaches, such as neural network and Gaussian process regression, reduce the need for prior dynamic knowledge, but require extensive data collection and training[23–26]. The Koopman operator[27, 28] offers a promising alternative by capturing nonlinear dynamics through linear evolutions in an infinite-dimensional embedding space. Finite-dimensional approximations of Koopman models are commonly integrated with the linear quadratic regulator (LQR)[7] and model predictive control (MPC)[29], enabling efficient controller synthesis. Among them, Koopman-based MPC has demonstrated its effectiveness in the control of soft robots, but mainly in quasi-static space[30–33]. A recent configuration-specific Koopman-based control approach advanced a soft robotic arm operating in an inertial dynamic regime through time-delay embeddings[7]. Despite these advances, the aforementioned approaches require repetitive modelling and controller design to adapt to new configurations, limiting their practical applicability in reconfigurable robotic systems.

The second challenge is the rapid generation of policies to accommodate dynamic variations in multiple configurations. Although reinforcement learning (RL) offers a promising model-free policy design approach[34–37], prevalent RL algorithms face high sample complexity, particularly in continuous control tasks[38, 39]. This high sample demand is costly for real-world training, due to the delicate nature and susceptibility to wear and tear of soft robots[40]. Although physical simulators provide an alternative to real-world training, RL algorithms such as deep deterministic policy gradient[41] and proximal policy optimization[42] still require millions of data to converge[38]. Moreover, building high-fidelity simulators of soft robots is challenging due to their nonlinear, configuration-dependent dynamics, exacerbating the sim-to-real gap.

In this work, we introduce a generalizable control system that enables fast adaptation across diverse configurations in soft robots (Fig. 1). Our system consists of two key modules: (a) a linear embedding RL (LERL) framework that learns control policies within a linear Koopman embedding space for fast multi-configuration adaptation (Fig. 1a), and (b) three types of soft robot platforms with diverse configurations for experimental validation, including an elephant-trunk-shaped robot, a soft-muscle robot, and a worm-like robot (Fig. 1b-d). These robot configurations feature diverse materials, stiffnesses, structural geometries, and assembly patterns. The presented LERL framework is built upon the hypothesis that different soft robot configurations share fundamental but also exhibit configuration-dependent dynamic characteristics. We demonstrate that by mapping these shared dynamics into a unified linear embedding space and performing policy adaptation online within this space, control policies could be quickly transferred across diverse configurations.

We validated our system experimentally across 30 robot configurations, including 22 variations of elephant-trunk robots, three soft-muscle robot variants, three worm-like robots, and two hybrid-assembled robots combining honeycomb and soft-muscle segments (Fig. 1a and Fig. 8). The experimental results demonstrate that LERL achieves

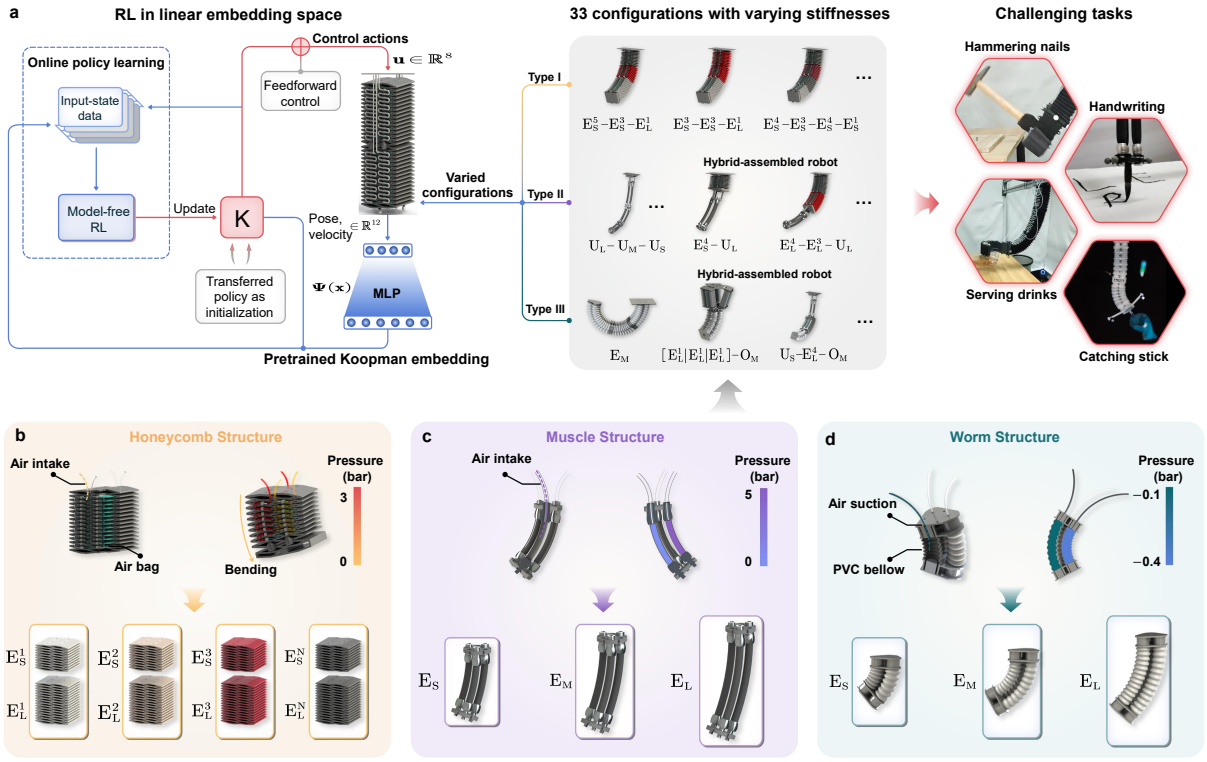

Fig. 1: **Our generalizable control system across 30 configurations with diverse materials and stiffnesses.** **a**, A generalizable control system with fast adaptability across multiple configurations and tasks. The Koopman embedding $\Psi(x)$ is offline trained only once on a fixed configuration, and the policy gain matrix K is online updated for multi-configuration adaptation via model-free RL in the Koopman embedding space. **b**, Type I elephant-trunk robots: Each segment features a honeycomb structure with four pneumatic actuators. Honeycomb segments' properties vary with wall thicknesses (superscript indices $1 \cdots N$ denote wall thickness affecting the stiffness) and lengths (subscript indices 'S, M, L' represent segment lengths: Short, Medium, and Long). **c**, Type II soft-muscle robots: Each segment is composed of three parallel pneumatic muscles, each driven by a pneumatic actuator. **d**, Type III worm robots: Each segment features a worm structure with three pneumatic actuators.

a 75× reduction in training samples while maintaining robust performance in challenging conditions, including high-payload manipulation (1 kg), high-speed motion (Worm: 1.89 $\mathrm{m \cdot s^{-1}}$; Elephant-trunk: 0.78 $\mathrm{m \cdot s^{-1}}$), and multi-actuator fault scenarios (Table 1). Critically, LERL enables rapid policy transfer to execute diverse tasks (Fig. 1d), allowing a base policy with online updates to empower robots performing previously unattainable real-world skills, including carpenter-inspired nail hammering into wooden boards, bartender-like drinks serving with safe human-robot interaction, fluid calligraphy brush handwriting, and quick hand-eye reaction games mimicking athletic and child training. The presented work represents a step toward a generalizable control framework that enables rapid multi-configuration adaptation in soft robots. Through online data-efficient RL within a pretrained Koopman embedding space, our proposed system decouples control policies from specific configurations, bridging mechanical reconfigurability and control flexibility. This work may also inspire policy transfer and adaptation solutions for other physical systems with shared fundamental dynamic characteristics.

Linear embedding RL framework

LERL formulates control policy learning in a pretrained linear embedding space, allowing computationally and data efficient online policy learning across diverse configurations (Fig. 2). The initial step involves pretraining

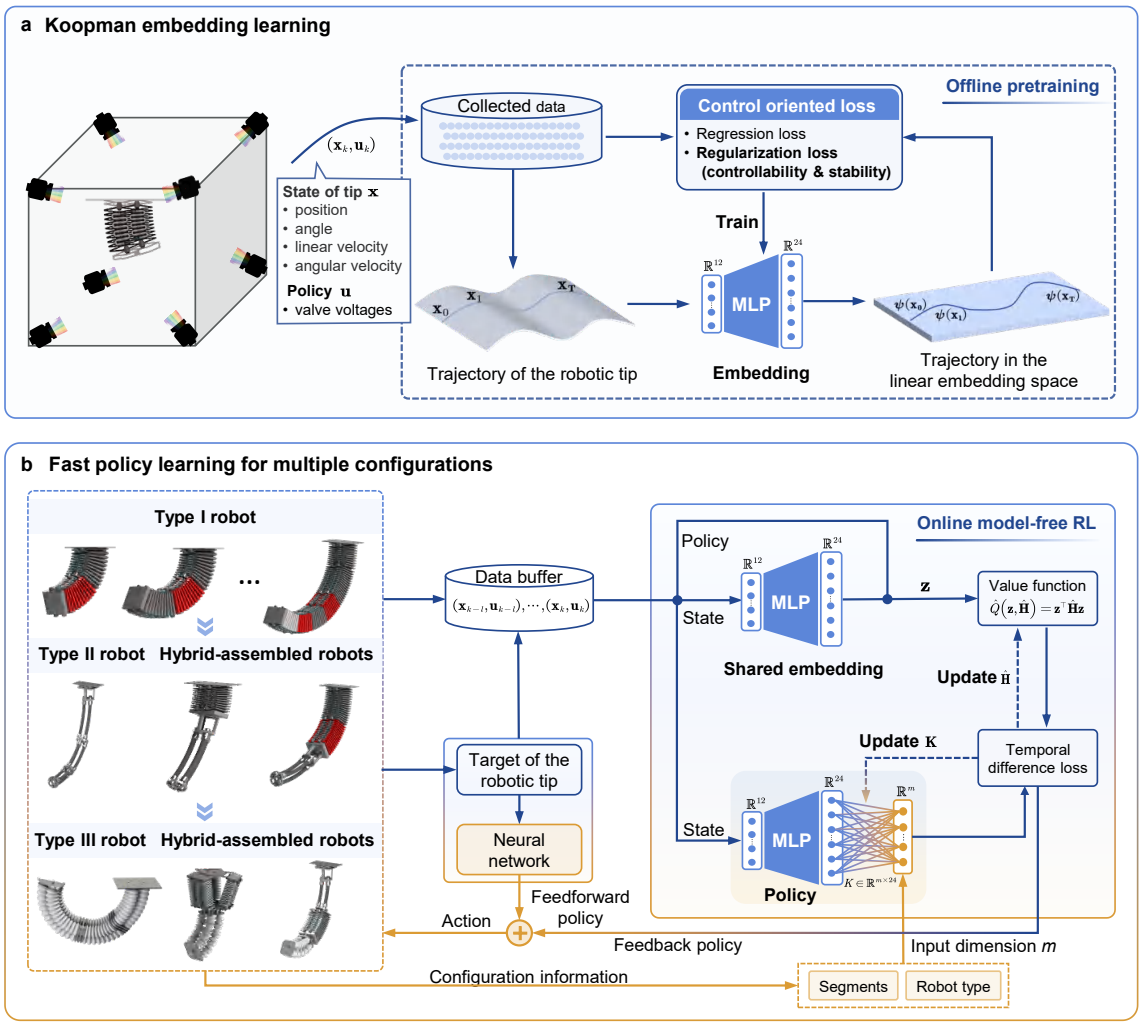

Fig. 2: **Linear embedding RL framework. a**, The Koopman embedding is trained offline with precollected input-state samples from the single honeycomb segment E_S^1. **b**, Online policy learning is conducted in the linear embedding space using model-free RL across multiple configurations with diverse materials, stiffnesses, structural geometries, and assembly pattern, where the pretrained Koopman embedding is shared for all new configurations.

a multilayer perceptron (MLP)-based Koopman embedding $\Psi(x)$ using input-state data collected from a single honeycomb segment (E_S^1), where $x \in \mathbb{R}^{12}$ represents the pose (position and orientation) and velocity (linear and angular velocities) of the robot tip (Methods and Supplementary Section 1). The Koopman embedding maps the evolution of the robot tip's pose and velocity to a higher-dimensional, inherently linear space (Fig. 2a). In Koopman embedding learning, we introduce control-oriented regularization techniques along with regression objectives to ensure key open-loop control properties (stability and controllability) in the embedding space, which are crucial for closed-loop performance.

With pretrained Koopman embedding, model-free RL is employed to update policies online in the linear embedding space (Fig. 2b). The Koopman embedding and control policy are then transferred across configurations, facilitating real-time policy adaptation for diverse configurations in the unified linear embedding space. To address different adaptation scenarios, we introduce two variants of our method: LERL and LERL-transfer. LERL trains the policy from scratch using a pretrained configuration-specific Koopman embedding. LERL-transfer extends

Table 1: Comparison with state-of-the-art (SOTA) methods for control of soft robots. Our LERL framework enables policy transfer across 30 distinct configurations, whereas most SOTA methods are limited to a fixed configuration. With just 2k samples for policy transfer, LERL uses substantially fewer resources than RL methods such as proximal policy optimization (PPO)[42] (≥5250k, 2600× more), trust region policy optimization (TRPO)[43] (≥300k, 150× more), and deep deterministic policy gradient (DDPG)[41] (≥100k, 50× more). Additionally, KCID with time-delay (TD) embeddings[7] requires 18k samples per configuration, which is 9× more than LERL with MLP embeddings. When both using the same MLP embeddings, KCID demands 75× more samples than LERL. Despite using the fewest samples, LERL outperforms all other SOTA methods in terms of speed, acceleration, and payload capacity. LSTM: Long short-term memory; RNN: Recurrent neural network.

Work	**Method**	**Config.**	**Config. transfer**	**Robot type**	**Hybrid assembly**	**Online learning**	**Sample**	**Speed** $(\mathrm{m}\cdot\mathrm{s}^{-1})$	**Accel** $(\mathrm{m}\cdot\mathrm{s}^{-2})$	**Max Load** (g)
Ours	LERL	30	29	3	✓	✓	2k (transfer)	Type I: 0.78	11.9	1000
								Type III: 1.89	22.34	200
Ref[43]	LSTM + TRPO	1	-	1	✗	✗	≥300k	0.17	-	165
Ref[40]	RNN + RL	1	-	1	✗	✗	28k	-	-	105
Ref[42]	LSTM+PPO	1	-	1	✗	✓	≥ 5250k	0.3	-	-
Ref[41]	DDPG	1	-	1	✗	✗	≥ 100k	-	-	20
Ref[44]	Q-learning	1	-	1	✗	✗	20k	-	-	500
Ref[7]	KCID	2	-	1	✗	✗	TD: 18k / MLP: 150k	1.52	11.6	-
Ref[33]	Koopman + MPC	1	-	1	✗	✗	247k	-	-	-
Ref[31]	Koopman + MPC	1	-	1	✗	✗	≥43k	-	-	-
Ref[30]	Koopman + MPC	1	-	1	✗	✗	≥325k	-	-	275
Ref[23]	Hybrid model + PID	1	-	1	✗	✗	120k	0.08	0.07	-

LERL by incorporating policy transfer, beginning with a pretrained policy and Koopman embedding from one configuration, and subsequently updating the policy online to adapt to new configurations.

Results

In this section, we conducted comprehensive experiments to validate the generalizability and adaptability of our control system. The first experiment was to validate the pretrained Koopman embedding and online policy learning performance on one configuration. In subsequent experiments, the policy was transferred to control 30 distinct configurations, with comprehensive validations across all cases. Throughout the experimental study, we compared our approach with the Koopman control method with inertial dynamics (KCID)[7], a state-of-the-art solution for dynamic control of soft robots with fixed configurations. KCID is limited by its reliance on configuration-specific modelling of soft robots. In contrast, our method is configuration-agnostic, achieving a 75× reduction in training samples and eliminating the bottlenecks of repetitive modelling when adapting to new configurations. Finally, the control policy was transferred across diverse configurations to accomplish real-word challenging tasks previously unattainable for soft robots, including carpenter-inspired nail hammering, bartender-like drinks serving, fluid calligraphy brush handwriting, and quick hand-eye reaction games.

Policy learning performance in a single configuration

An MLP-based Koopman embedding $\Psi(x)$ was first trained in a configuration (honeycomb segment $\mathrm{E}_{\mathrm{S}}^{1}$) with control-oriented regularization (Methods and Supplementary Section 1). As demonstrated in Fig. 3a, applying control-oriented regularization during the pretraining phase produces an open-loop stable Koopman model, characterized by smaller-magnitude eigenvalues positioned farther from the unit circle compared to unregularized models.

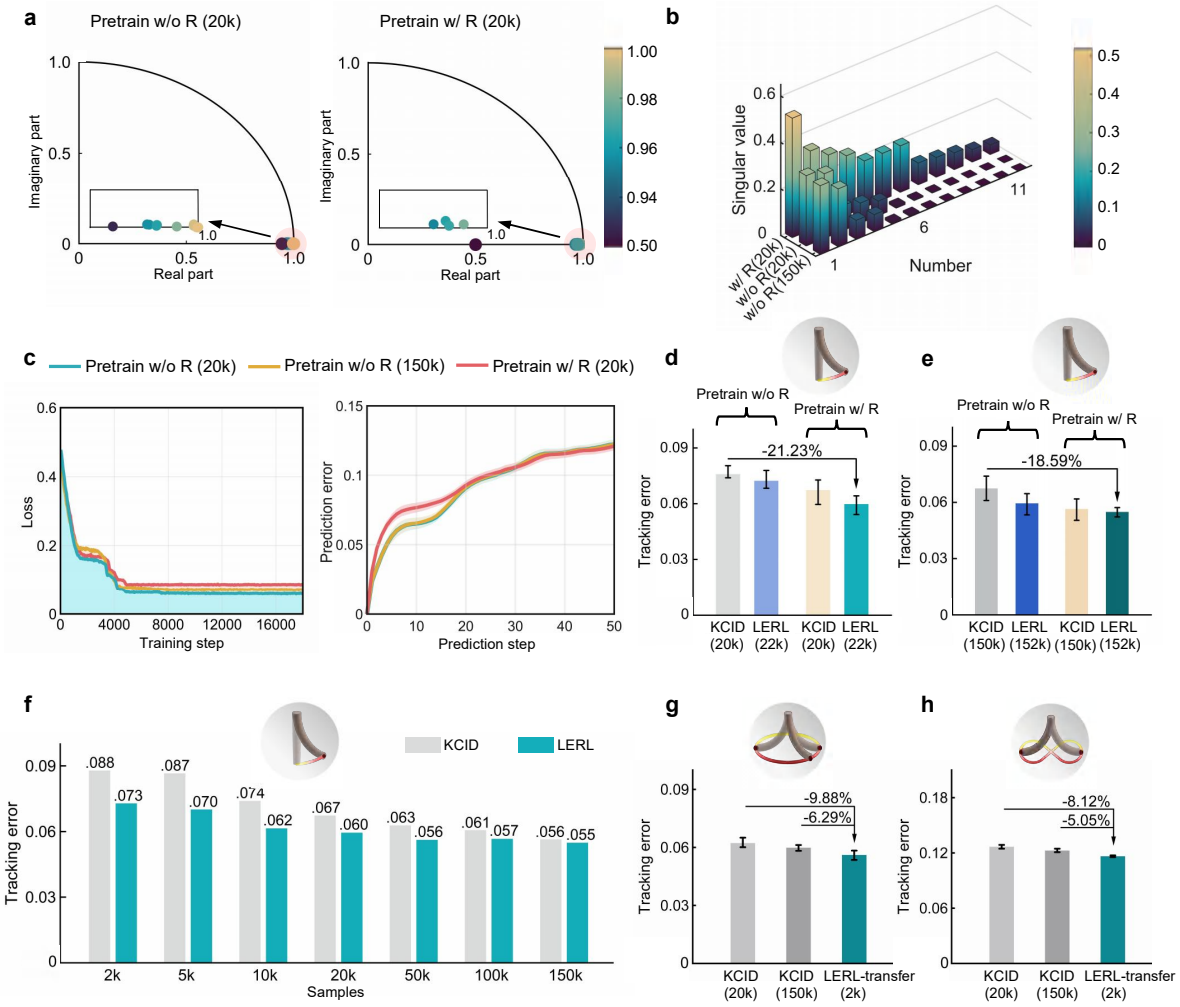

Fig. 3: **Offline Koopman embedding training and online policy learning for honeycomb segment E_S^1. a**, The open-loop eigenvalue plots for Koopman models pretrained with (w/) or without (w/o) regularization (R). The eigenvalues pretrained w/ regularization locate farther from the unit circle, resulting in a larger stability margin; 20k=20000. **b**, The singular value distribution (SVD) of the controllability matrix of Koopman models. Pretraining w/ regularization leads to SVDs with higher magnitudes. **c**, The training loss (equation (5) in Methods) and prediction error of the Koopman model, Prediction error $:= \sqrt{\frac{1}{L}\sum_{l=1}^{L}\|x_l - \hat{x}_l\|^2}$, L denotes the amount of samples. **d**-**e**, Performance comparison of KCID and LERL during pretraining w/ or w/o regularization, Tracking error $:= \frac{1}{M\cdot N}\sum_{i=1}^{M}\sum_{k=1}^{N}\left\|\bar{x}_{i,k} - \bar{x}_{r,i,k}\right\|^2$, $\bar{x}$, $\bar{x}_r \in \mathbb{R}^{12}$ are the normalized real state variable (pose and velocity) and its reference, N is the algorithm horizon, and $M = 5$ is the number of experiments. **f**, Sample comparison of LERL and KCID in target reaching. **g**-**h**, Performance comparison in policy transfer to circular and bow tie tracking.

In addition, it preserves state prediction errors comparable to the unregularized case (Fig. 3c), while enlarging the singular values of the controllability matrix (Fig. 3b). The enhanced open-loop stability and controllability address the gap between data-driven modelling and closed-loop control.

With the pretrained Koopman embedding, model-free RL is employed to update policies online in the linear embedding space. The control policies within the pretrained embedding space were generated using 2000 (2k) samples: 500 samples for offline feedforward policy generation (Fig. 2b; Methods and Supplementary Section 2) and 1.5k samples for online feedback policy training (Methods and Supplementary Section 4). As demonstrated in

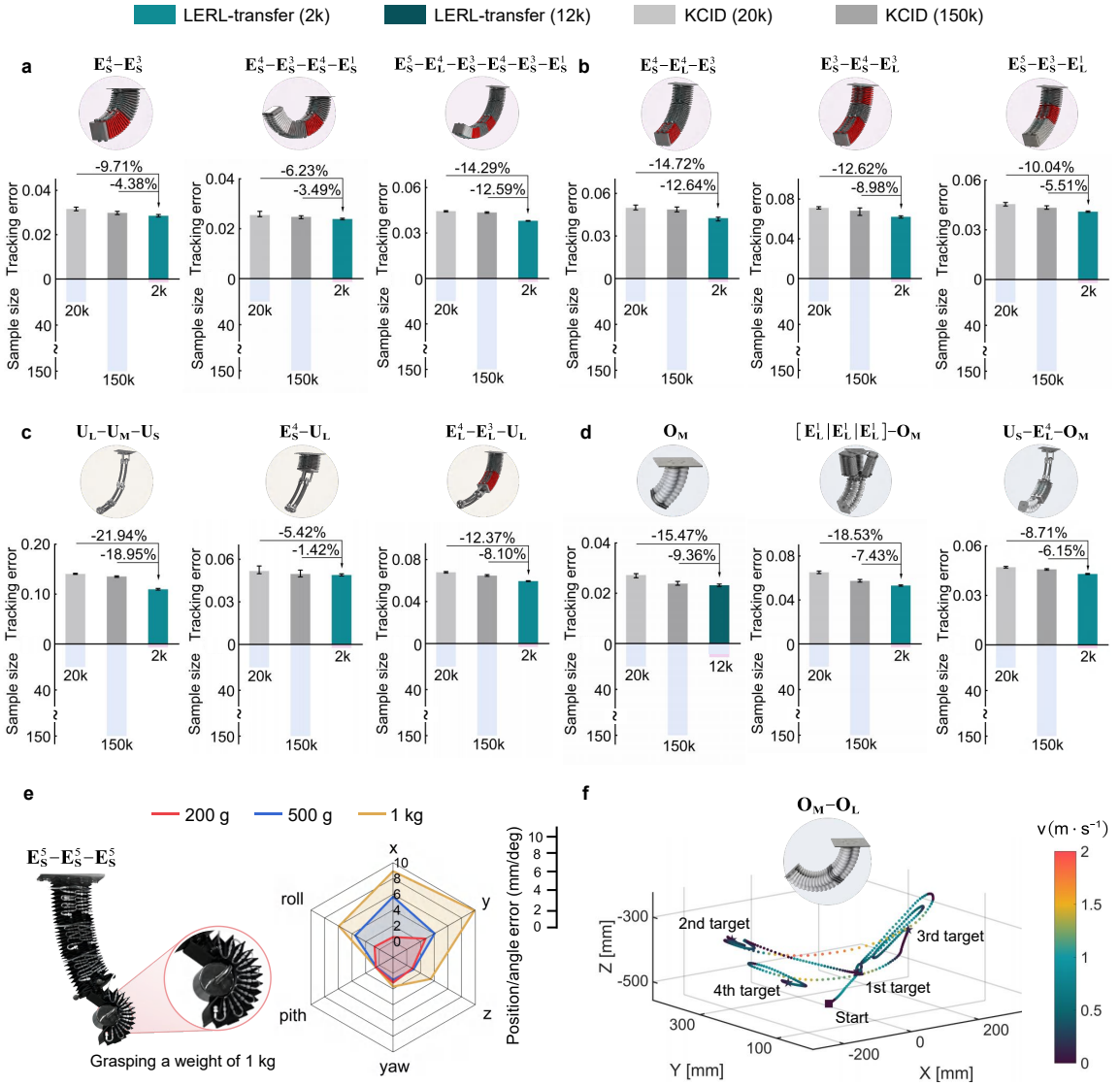

Fig. 4: **Policy adaptation performance to multiple configurations of three soft robot prototypes.** **a**, Policy adaptation to elephant-trunk robots with multiple segments. **b**, Policy adaptation to elephant-trunk robots under diverse assembly configurations. **c**, Policy adaptation to soft-muscle and hybrid-assembled robots. **d**, Policy adaptation to worm robots. **e**, Empirical robustness under different loads (200 g, 500 g, 1 kg) and visualization of the robot grasping a 1 kg weight to the target position. **f**, The worm robot in configuration E_M-E_L tracks targets with a maximum velocity up to 1.89 $m \cdot s^{-1}$.

Fig. 3, LERL using 22k training samples, 20k for offline Koopman embedding training and 2k for policy generation (rightmost bar, Fig. 3d), achieves an 11.37% reduction in tracking error compared to KCID with 150k samples (leftmost bar, Fig. 3e); and results in a steady-state position error of 0.32 mm, nearly 4× smaller than KCID's 1.26 mm. The comparison under multiple sample conditions in Fig. 3f demonstrates a substantial sample reduction of LERL over KCID even when the configuration is unchanged. Specifically, LERL with 20k pretraining samples performs on par with KCID using 100k pretraining samples, reducing training data by 5× in a fixed configuration. For new tasks, LERL-transfer can further refine the transferred policy online with just 2k samples, surpassing KCID in both control performance and sample efficiency (Figs. 3g-h).

Policy adaptation performance in multiple configurations

The Koopman embedding $\Psi(x)$, pretrained in the configuration E_S^1 using 20k training samples, was reused in new configurations without retraining. The learned policy was transferred and updated online to adapt to dynamic variations in multiple configurations. Fig. 4 shows the results of LERL-transfer and KCID for circular tracking in 12 distinct configurations, while auxiliary results for target reaching and bow tie tracking in 18 configurations are given in Figs. 9 and 10, and Supplementary Video 5.

Policy adaptation from one segment to more. The control policy initially trained in E_S^1 was efficiently transferred using a padding procedure detailed in Supplementary Section 5, and refined online to adapt to new configurations comprising two, three, and four segments. As shown in Fig. 4a, LERL-transfer with 2k samples achieves lower tracking errors in all scenarios compared to KCID with 150k samples, reducing the sample size by 75×.

Policy adaptation under diverse assembly configurations. We demonstrate the rapid policy adaptability to the three-segment elephant-trunk robot with various assembly configurations in Fig. 4b, wherein LERL-transfer costing 2k samples outperforms KCID with 20k and 150k samples. Compared to KCID with 150k samples, our method reduces training samples by 75×, while achieving a reduction of 5.51%-12.64% in the tracking error. We also evaluate the empirical robustness of LERL in the configuration E_S^5-E_S^5-E_S^5 under different loads (200 g, 500 g, 1 kg), as shown in Fig. 4e and Supplementary Video 6. The position and angle of the robot tip eventually converge to the target with a steady-state position error of 0.48 mm under a payload of 200 g and with a steady-state position error of 10.07 mm under a payload of 1 kg (Fig. 6c).

Policy adaptation to soft-muscle and hybrid-assembled robots. We further validate LERL's versatility by transferring the control policy to heterogeneous soft-muscle robots and hybrid-assembled robots (Fig. 4c). Although the actuator numbers of soft-muscle segments differ from those of honeycomb segments, the learned policies are directly transferable via an action re-allocation strategy (Supplementary Section 5). The hybrid-assembled robots, composed of honeycomb and soft-muscle segments, exhibit substantial differences in materials, structures, and actuations (Fig. 1b and c). Nevertheless, LERL-transfer with only 2k samples enables hybrid-assembled robots to successfully complete tracking tasks, achieving an 8.10% reduction in tracking error compared to KCID with 150k samples (Fig. 4c). These results highlight LERL's potential for rapid policy adaptation across heterogeneous robots with distinct dynamic characteristics.

Policy adaptation to worm robots. During policy adaptation to the worm segment E_M, the Koopman embedding pretrained on the honeycomb segment is reused. An offline policy initialization procedure (see Supplementary Section 7) was conducted using 10k samples, as direct policy transfer from the elephant-trunk robot is infeasible due to different actuation modes (positive vs. negative pressure; Fig. 1b and d). As shown in Fig. 4d, LERL-transfer with 12k samples (10k were used for offline policy initialization) outperforms KCID with 20k and 150k samples. In policy adaptation to worm robots with two and three segments, the online learned policy using 2k samples outperforms KCID with 150k samples, reducing the sample size by 75× (Fig. 4d). Furthermore, in the worm robot with configuration E_M-E_L, LERL achieves position tracking with a steady-state position error of 3.22 mm while operating at the extreme condition (Fig. 4f) with velocities and accelerations up to 1.89 $m \cdot s^{-1}$ and 22.34 $m \cdot s^{-2}$ (Table 1), which are 24% and 92% higher than the previously recorded[7] velocity of 1.52 $m \cdot s^{-1}$ and acceleration of 11.6 $m \cdot s^{-2}$.

Hammering nails

No previous work on soft robots has successfully utilized a hammer to drive nails for binding wooden boards, like a skilled carpenter. This challenging task demands high payload capacity and precise control at high speeds to generate sufficient force for driving nails. The LERL policy, transferred from the segment E_S^1 with online updates, has achieved precise control of a 370 g weighted hammer grasped by the elephant-trunk robot (Fig. 5a), striking nails to bind two wooden boards. During the experiment, the robot tip's pose and velocity were measured using a motion-capture system. The measured data was then used as input to the policy network to generate control actions. As shown in Figs. 5b-c and Supplementary Video 1, at the beginning of the task, the elephant-trunk robot was controlled to grip the hammer handed to it by a human. The robot then used the hammer to quickly drive nails into both sides of the wooden board, completing the task in 72 seconds, reaching a maximum speed of 0.78 $m \cdot s^{-1}$,

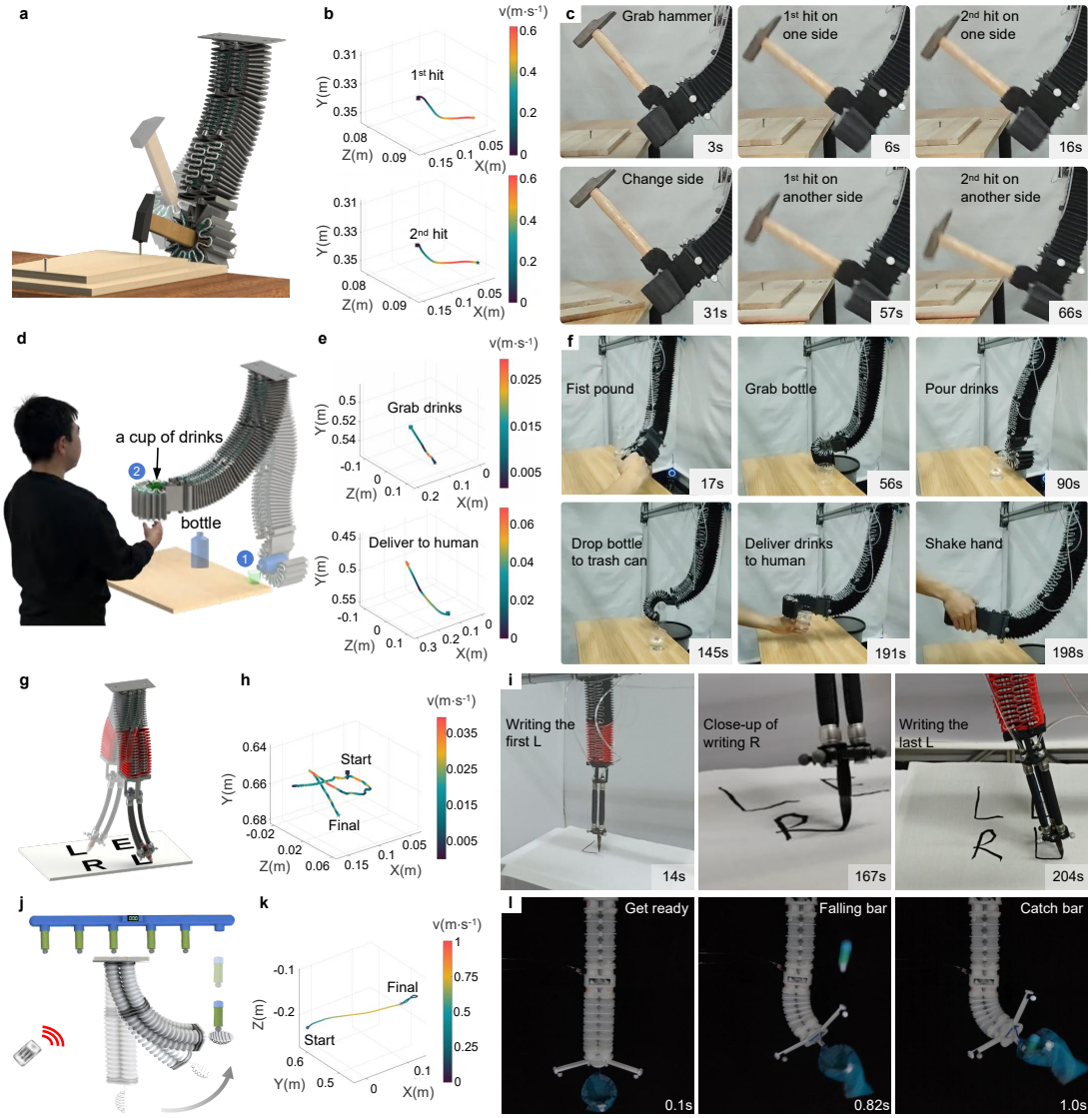

Fig. 5: **Completing challenging tasks with LERL-empowered soft robots.** **a**-**c**, The elephant-trunk soft robot drives nails to bind two wooden boards: scene **a**, highlighted trajectory **b**, and snapshots **c**. **d**-**f**, The elephant-trunk robot autonomously serves drinks to a human with safe human-robot interactions: scene **d**, highlighted trajectory **e**, and snapshots **f**. **g**-**i**, The hybrid-assembled robot performs calligraphy brush handwriting: scene **g**, highlighted trajectory **h**, and snapshots **i**. **j**-**l**, The worm robot mimics human to play a quick hand-eye reaction game: scene **j**, highlighted trajectory **k**, and snapshots **l**.

and achieving an acceleration of 11.6 $\mathrm{m} \cdot \mathrm{s}^{-2}$. This task expands the capabilities of soft robots for daily assistive and industrial applications.

Serving drinks with safe interactions

With the rise of embodied intelligence, there has been growing interest in enhancing the intelligent manipulation capabilities of robotic arms, focusing primarily on rigid body designs[45]. However, soft robots provide safer human-robot interactions compared to rigid robots, as rigid bodies with intelligent algorithms do not ensure absolute safety. Our transferred LERL policy enabled the elephant-trunk robot to perform the drinks-serving task with precise and

smooth operation (Fig. 5d), emulating the actions of a skilled human bartender. As demonstrated in Figs. 5e-f and Supplementary Video 2, the soft robot interacts with the human safely through a fist bump and handshake, adaptively adjusts its position and orientation to pour drinks smoothly into the cup, throws the cup into the trash can, and hands the cup to the guest gently and safely. In addition, the robot can maintain stable operation under external human intervention (Supplementary Video 2) through online policy updates. This task demonstrates our approach's capability in adaptive control of soft robots under dynamic loads, highlighting the potential in daily delicate task operations that require safe human-robot interactions.

Calligraphy brush handwriting

Calligraphy handwriting with soft arms and brushes is a challenging task. It requires the soft arm and brush to precisely adjust their movements to adapt to the dynamic pressure, speed, and angle required for fluid and clear strokes, while ensuring stability in each brushstroke. Our transferred LERL policy enables the hybrid-assembled soft robot to achieve smooth handwriting (Fig. 5g), overcoming the challenges of high-precision control posed by dynamic variations across different segment types. It ensures that the brush tip, mounted at the robot's end, accurately and stably hovers at a specific height above the paper while precisely following the character strokes. This avoids distortion or blurring of characters due to excessive force (caused by low height) or uneven speed, as demonstrated in Fig. 5h-i and Supplementary Video 3. This result highlights the capability of our framework to enable hybrid soft robots with soft brushes to achieve handwriting capabilities previously demonstrated only by rigid robots with rigid pens.

Quick hand-eye reaction game

The control capabilities under high-speed conditions were evaluated on the worm robot for a challenging hand-eye reaction game (Fig. 5j). This task is commonly used by athletes and children to train hand-eye reaction and coordination speeds. An autonomous machine equipped with sticks is hanging at a height of 0.48 meters above the robot, and the sticks are free to fall in an unknown and random order. A camera detects the movements of sticks to determine which stick falls. The soft robot is equipped with a net pocket at its tip, which moves quickly to catch the free-fall stick within 100 ms. The robot with the transferred LERL policy reached speeds of up to 1 $\mathrm{m} \cdot \mathrm{s}^{-1}$ and intercepted all free-fall sticks (Figs. 5k-l, Supplementary Video 4). This result demonstrates the potential of our LERL framework for challenging tasks that require high-performing control in high-speed conditions.

Discussion

This work presents a generalizable control system that achieves unprecedented policy adaptation across 30 distinct soft robot configurations, effectively bridging the longstanding gap between configuration versatility and scalable real-world deployment. By overcoming key limitations in configuration-specific modelling and control, our system addresses one of the primary barriers to the practical application of soft robotics[12].

Conventional model-based approaches demand extensive dynamical remodelling for each new configuration, while model-free RL methods typically require either data-intensive real-world interactions or high-fidelity simulators, which are especially challenging to construct for soft robots due to their nonlinear and configuration-dependent dynamics. In contrast, our method achieves rapid adaptation without configuration-specific modelling or controller redesign, enabled by three critical factors. First, the fundamental dynamic characteristics of soft robots are encoded into a unified, pretrained linear latent space, transforming configuration-dependent nonlinear dynamics into structured, approximately linear variations within this shared space. Second, these variations are efficiently addressed through an online, data-efficient RL algorithm, eliminating the need for configuration-specific remodelling and retraining. This approach achieves superior performance while requiring 75× fewer training samples than prior methods, and operates with real-time efficiency (see Table 2). Third, our control policy is directly learned and updated within the linear embedding space, mitigating the modelling–control gap that often undermines indirect optimal control strategies. As detailed in our theoretical analysis (Supplementary Section 8), this direct formulation substantially improves adaptation speed and control performance.

The presented framework enables fast multi-configuration adaptation across 30 configurations, demonstrating capabilities ranging from high-payload manipulation (1 kg) to rapid locomotion (1.89 $\mathrm{m} \cdot \mathrm{s}^{-1}$) and human-like

skills such as bartending, carpentry, brush calligraphy, and quick hand-eye reaction. Unlike existing configuration-specific controllers, our method dynamically updates policies online in response to configuration changes, emulating the adaptability observed in natural organisms. We believe this paradigm of online RL within a pretrained Koopman embedding space has the potential to establish future "foundation" control strategies of heterogeneous robotic systems. This includes unified and adaptable control of both rigid and soft robots (see Supplementary Section 6 for an elementary validation of rigid robots).

The demonstrated effectiveness on multiple platforms suggests a broad impact potential in the medical, industrial, and exploratory domains, laying the foundation for the development of agile, embodied intelligent systems[4] capable of configuration adaptability. Furthermore, the real-time efficiency of policy training facilitates rapid deployment in time-sensitive applications such as surgical robotics, where rapid adaptation is essential for operational efficiency.

Methods

Soft robotic platforms

We developed three distinct types of soft robotic platforms for experimental validation, each differing in materials, stifnesses, structures, and actuation modes.

Type I soft robotic platform. The Type I soft robotic platform features an elephant-trunk-shaped arm with a modular honeycomb segment architecture. We engineered 22 unique configurations by systematically varying four key parameters: segment length, stiffness, quantity, and assembly sequence (Fig. 8). For motion control implementation, the Type I soft robotic platform (Fig. 7a) integrates a motion capture module (Luster Swift30A) to measure the pose and velocity of the marked robot tip. The controller is implemented in Python on a CPU (Intel Core i9-13900HX), calculating control actions (50Hz) with measured real-time data related to the robot tip. These control actions are sent via a dSPACE MicroLabBox[46] to proportional valves (SMC ITV2030-212CL), which regulate the airflow to inflate airbags, driving the arm's deflection and extension.

Type II soft robotic platform. Each segment of the Type II robot consists of three parallel pneumatic muscles. Type II soft robotic platform includes three soft-muscle robots and two hybrid soft robots assembled using honeycomb and soft-muscle segments in varying orders and quantities (Fig. 8). The Type II soft robotic platform shares the same motion capture module and computing unit as the Type I platform (Fig. 7a).

Type III soft robotic platform. Type III robots use a worm-like segment structure, including three configurations ranging from one to three segments (Fig. 8). The Type III soft robotic platform (Fig. 7b) utilizes the same motion capture module but implements the controller in C++ on a CPU (Intel Core i9-13900HX). The calculated actions (50 Hz) are sent to an Arduino Mega 2560 microcontroller, generating analog signals to control vacuum proportional valves (HETIAN ITV2090-212CL5) connected to a vacuum pump. The valve control modulates the air chamber pressure, enabling dynamic arm deflection.

Overview of the LERL methodology

Our three types of soft robotic platforms, encompassing 30 distinct configurations (Fig. 8), are capable of executing diverse complex tasks. Although the fundamental control objective remains consistent across configurations—precise trajectory tracking through robotic tip manipulation—developing a generalizable controller with multi-configuration adaptability presents substantial challenges. Prior approaches, including model-based controllers[7, 30–33] and data-driven RL methods[38, 41, 42], demonstrate limitations in policy adaptation due to labor-intensive remodelling requirements and persistent sim-to-real transfer gaps.

Here, we present a data efficient LERL framework (Fig. 2), which captures intricate dynamic characteristics through Koopman operators and employs online model-free RL to adapt to dynamic variations across multiple configurations. This framework offers two key features: First, it enables online model-free policy learning in the linear Koopman embedding space, facilitating rapid and data-efficient adaptation to new robot configurations without the computational burden of dynamics remodelling or parameter retraining. Second, conventional modelling and control approaches often neglect the modelling errors that are intrinsic parts of robot dynamics or treat them merely as disturbances to be rejected, degrading control performance. In contrast, our method implicitly incorporates these modelling errors through direct policy optimization (as shown later in equation (9)), improving rather than degrading control performance.

Our methodology begins with data-driven training of the Koopman embedding from a single honeycomb segment, which maps the tip's pose and velocity into a linear embedding space (Fig. 2a). Building upon this, a data efficient RL algorithm is deployed to update control policies in real-time to address configuration-specific dynamic variations, enabling rapid adaptation across diverse configurations via a base policy with online updates (Fig. 2b).

Offline Koopman embedding training

This section outlines the offline training process for the shared Koopman embedding, which captures the fundamental dynamics of soft robots. First, training data from a single honeycomb robot segment are collected and normalized. Then, we construct the Koopman embedding function using an MLP and introduce the associated loss functions along with control-oriented regularizations to guide the training of the Koopman embedding.

Training data generation. We collected 20k samples of the input-state pair $\{x, u\}$ from the single honeycomb

segment E_S^1 under sinusoidal excitation. The control input $u \in \mathbb{R}^4$ regulates the voltage applied to four proportional valves. The state of the robot tip is $x = \left[p_x, p_y, p_z, v_x, v_y, v_z, \theta_x, \theta_y, \theta_z, w_x, w_y, w_z\right]^\top \in \mathbb{R}^{12}$ that captures the complete kinematic and dynamic profile of the robot tip, where $p_\star$, $v_\star$, $\theta_\star$, $w_\star$ represent the Cartesian coordinates of position, linear velocity, orientation angle, and angular velocity, respectively ($\star \in x, y, z$). The state and control are normalized to the intervals $[-1, 1]$ and $[0, 1]$ for training.

Embedding construction. Koopman operators typically capture the intricate characteristics of nonlinear dynamics through observations in a linear embedding space. Consider a discrete-time dynamics model of soft robots: $x^+ = f(x, u)$, where x, $x^+ \in \mathbb{R}^n$ are the current and subsequent states sampled in a time interval t_s; the control $u \in \mathbb{R}^m$; f is a state transition function. Let $u_\infty = \{u(i)\}_1^\infty$ be the collection of all control inputs in the control space, and Γ be a left shift operator such that $u_\infty(k+1) = \Gamma u_\infty(k)$[47]. An infinite-dimensional Koopman operator $\mathcal{K}$, acting on a scalar-valued observable $\psi(x, u_\infty)$, is defined as[47, 48] $\mathcal{K}\psi(x, u_\infty) = \psi(x, u_\infty) \circ (f(x, u_\infty(0)), \Gamma u_\infty)$. The finite-dimensional approximation of $\mathcal{K}$ is typically derived using dynamic mode decomposition with controls[27], where a predefined collection of Koopman observables $\Psi(x, u) = (\Psi(x), u) \in \mathbb{R}^{n_\psi + m}$ is used, $\Psi(x) \in \mathbb{R}^{n_\psi}$ is usually selected as basis functions.

Here, we adopt a trainable MLP for an enhanced representation of the embedding function $\Psi(x)$, with alternative approaches including Gaussian kernel functions and time-delay embeddings investigated in our ablation studies (Fig. 6). Letting $s = \Psi(x)$ be the lifted embedding state, one writes the Koopman model[29] as

$$s^+ = As + Bu + w(s, u), \tag{1}$$

where A and B are the model parameters to be learned[48], $w(s, u)$ is the residual modelling uncertainty.

Although conventional implementations typically incorporate the state x as prior knowledge in constructing $\Psi(x)$, such methods often result in a dense state transition matrix A with limited spectral regularization[29]. Hence, we introduce a trainable transformation matrix $T \in \mathbb{R}^{12\times12}$ that projects the state x into a structured eigenspace, allowing for direct manipulation of eigenvalues. The resulting Koopman embedding is designed as

$$\Psi(x) = (Tx, \bar{\Psi}(Tx)), \tag{2}$$

where $\bar{\Psi}(Tx)$ is implemented using an MLP with a 12-64-128-64-12 network structure. Each hidden layer employs Rectified Linear Unit (ReLU) activation functions.

Loss functions. The standard loss functions in Koopman embedding training include linear regression loss (L_e), reconstruction loss (L_r), and regularization on the matrix T (L_T), detailed in Supplementary Section 1. To bridge the gap between regression accuracy and control performance, we introduce two control-oriented regularization terms: (a) eigenvalue regularization for open-loop stability guarantees and (b) singular value regularization for enhanced controllability. First, the sparse structure of A is explicitly designed, combining q parameterized real eigenvalues and $(n_\psi - q)/2$ conjugate eigenvalue pairs. Specifically, the regularization loss for A is formulated as

$$L_A = \sum_{j \in \mathcal{E}_A} \|\lambda(A)_j - \eta_1\|^2, \tag{3}$$

where $\lambda(A)_j$ represents the j-th eigenvalue of A, $\eta_1 < 1$; $\mathcal{E}_A$ is the collection of indices associated with eigenvalues that satisfy $\lambda(A)_j > \eta_1$.

With regularization term L_A, the eigenvalues of A could be restricted within the unit circle, achieving balance between regression accuracy and system stability. However, the controllability matrix $C := \left[B \; AB \; A^2B \; \cdots \; A^{n_\psi - 1}B\right]$ may exhibit undesirably small singular values corresponding to large eigenvalues of A, particularly those that lie within but approach the unit circle. This phenomenon can degrade closed-loop control performance and lead to suboptimal dynamic control behavior. Hence, we introduce an additional regularization loss term to shape the singular value distribution of C, formulated as

$$L_C = \sum_{j \in \mathcal{E}_C} \|\sigma(C)_j - \eta_2\|^2, \tag{4}$$

where $\sigma(C)_j$ is the j-th singular value of C, $\eta_2 > 0$; $\mathcal{E}_C$ is the collection of indices associated with singular values smaller than η_2.

The overall loss function used for training the Koopman embedding is as follows:

$$L = \alpha_1 L_e + \alpha_2 L_r + \alpha_3 L_T + \alpha_4 L_A + \alpha_5 L_C, \tag{5}$$

where $\alpha_i, i = 1, \cdots, 5$ are the tunable parameters to balance each loss function. Optimizing the loss in equation (5) generates the configuration-agnostic Koopman embedding $\Psi(x)$ along with the configuration-specific model parameters A and B in equation (1). Only $\Psi(x)$ is shared among diverse configurations for online policy adaptation.

Online model-free policy learning

This section presents the online, model-free policy learning approach with the shared configuration-agnostic Koopman embedding, enabling real-time and rapid adaptation to diverse new configurations. We first describe the policy design within the embedding space, followed by the learning process using a model-free Q-learning algorithm.

Policy design in the embedding space. Prior studies used an approximated nominal Koopman model $\hat{s}^+ = As+Bu$, to formulate LQR[7] and MPC[30] approaches for soft robots, which often neglects the effect of modelling uncertainty $w(s, u)$ existing in the real Koopman model (1). However, even a minor modelling uncertainty $w(s, u)$ can compromise the stabilizability of (A, B)[29]. Also, the Koopman model that best fits model training data could be suboptimal for controller design[49]. To address this issue, we directly learn the control policy in the linear embedding space through input-state data. The modelling uncertainty is hidden in the input-state data used during policy learning, which contributes to the policy optimization (proven in Section S8).

The control policy of LERL consists of a dynamic feedback policy and a feedforward policy:

$$u = u_e + u_r, \tag{6}$$

where $u_e = Ks_e$ represents the dynamic feedback policy through the gain matrix $K \in \mathbb{R}^{m\times n_\psi}$ acting on the linear embedding space spanned by $\Psi(x)$, $s_e = s - s_r$ denotes the lifted state error with $s_r = \Psi(x_r)$ being the lifted reference state; the feedforward policy u_r maintains the robot tip steadily at its reference state x_r, which is precalculated offline as introduced in Supplementary Section 2.

The gain matrix K is learned online by solving an optimal control problem as follows:

$$\min_{u_e} V(s_{e,0}) = \sum_{k=0}^{+\infty} \gamma^k l(s_{e,k}, u_{e,k}), \tag{7}$$

subject to a Koopman error model $s_e^+ = As_e + Bu_e + w_e(s_e, u_e)$ with $w_e(s_e, u_e) := w(s, u) - w(s_r, u_r)$, where $l(s_{e,k}, u_{e,k}) = \|s_{e,k}\|_Q^2 + \|u_{e,k}\|_R^2$; $Q \in \mathbb{R}^{n_\psi\times n_\psi}$, $R \in \mathbb{R}^{m\times m}$ are symmetric positive definite matrices; $0 < \gamma \leq 1$ is a discount factor.

To perform model-free RL, the so-called Q-function (state-action value function), i.e., $Q(z_k) := l(z_k) + \gamma V(As_{e,k} + Bu_{e,k} + w_{e,k})$, is written as

$$Q(z_k) = z_k^\top H_o z_k + G(z_k) := z_k^\top H z_k, \tag{8}$$

where $z_k := [s_{e,k}^\top,\ u_{e,k}^\top]^\top$; $H_o \in \mathbb{R}^{(m+n_\psi)\times(m+n_\psi)}$ and $H = \begin{bmatrix} H_{ss} & H_{su} \\ H_{us} & H_{uu} \end{bmatrix} \in \mathbb{R}^{(m+n_\psi)\times(m+n_\psi)}$ are unknown matrices; the term $G(z_k)$ originates from the modelling uncertainty $w(s, u)$ in equation (1). Since it is directly tied to the input-state pair, we leverage $G(z_k)$ to improve control performance, rather than treating it as an uncertainty that degrades performance[29]. Setting $\partial Q(z_k)/\partial u_{e,k} = 0$ with equation (8) yields the analytical expression of the

optimal feedback policy associated with H:

$$u_{e,k} = -H_{uu}^{-1} H_{us} s_{e,k}, \tag{9}$$

which contains the term $G(z_k)$ for control performance improvement.

Model-free policy learning. Here, we apply a model-free Q-learning algorithm to approximate the matrix H in equation (8) and generate the optimal feedback policy with equation (9) in the linear embedding space, directly from the online measured data $\{s_k, u_k\}$ and the target information $\{s_{r,k}, u_{r,k}\}$. We first construct a parameterized approximation of the Q-function in equation (8) as $\hat{Q}(z, h) = z^\top \hat{H} z = h^\top \mathcal{z}$, where $\mathcal{z} := z \otimes z$, and $h := \mathrm{vec}(\hat{H}) \in \mathbb{R}^{q(q+1)/2}$ is the vectorized form of $\hat{H}$, $q = n_\psi + m$. With an initialized $\hat{H}_0$, our method updates $\hat{H}$ so that $\hat{Q}(z, h)$ asymptotically converges to its optimal value. The optimal feedback policy is then naturally derived from the entries of $\hat{H}$ following equation (9).

At the i-th iteration, an estimate of the Q-function from equation (8) is calculated as $d(z_{i,k}, \hat{H}_i) = l(z_{i,k}) + \gamma \|z_{i,k+1}\|^2_{\hat{H}_i}$. Then, $h_{i+1} = \mathrm{vec}(\hat{H}_{i+1})$ is updated by minimizing the temporal difference loss as follows:

$$\min_{h_{i+1}} \sum_{j=k-1}^{k-N} \|h_{i+1}^\top \mathcal{z}_j - d(z_{i,j}, \hat{H}_i)\|^2. \tag{10}$$

Let $Z_k = [\mathcal{z}_{[k-N]} \cdots \mathcal{z}_{[k-1]}]$ be a collected dataset composed of the past N-step input-state pairs, where $\mathcal{z}_{[i]} = z_{[i]} \otimes z_{[i]}$. Solving equation (10) obtains:

$$h_{i+1} = (Z_k Z_k^\top)^{-1} Z_k M_k, \tag{11}$$

where $M_k = [d(\mathcal{z}_{[k-N]}, h_i) \cdots d(\mathcal{z}_{[k-1]}, h_i)]^\top$. The inverse operation in equation (11) requires that $Z_k Z_k^\top$ is of full rank. To meet this condition, the number N is selected greater than $q(q+1)/2$ and the policy with exploration noise n_e is adopted during the initial learning stage. If the matrix $Z_k Z_k^\top$ is full rank but ill-conditioned, calculating h_{i+1} may introduce substantial errors. To mitigate this issue in online deployment, we propose two alternative strategies: first, employing warm-start techniques during policy learning (Supplementary Section 3); and second, utilizing a gradient descent-based update rule, such as the Adam optimizer. The implementation procedures are deferred to Algorithm S1. The theoretical guarantee for the online policy learning outlined above is provided in Supplementary Section 8.

Integral action in policy learning. Offline training the feedforward policy u_r in equation (6) relies on precollected quasi-static motion data for each robot configuration. To facilitate rapid policy generation, limited quasi-static data is used, which may introduce inaccuracies and potentially degrade control performance. To mitigate this issue, we incorporate an integral action into policy learning to compensate for these inaccuracies. To this end, we define $\dot{q} = C_p s_e$, where $C_p = [I_6\ 0]$ and $q \in \mathbb{R}^6$ consist of the robot tip's position and angle. Discretizing $\dot{q}$ with a time interval t_s writes $q^+ = q + t_s C_p s_e$. Defining an extended state $e_a := [s_e^\top, q^\top]^\top$, one writes the augmented model as

$$e_a^+ = A_a e_a + B_a u_e + E_a w_e, \tag{12}$$

where $A_a = [A_1^\top\ A_2^\top]^\top$, $A_1 = [A\ 0]$, $A_2 = [t_s C_p\ I_6]$, $B_a = [B^\top\ 0]^\top$, and $E_a = [I\ 0]^\top$. Implementing Algorithm S1 with this augmented model generates the dynamic feedback policy u_e that includes an integral action on the robot tip's pose error to compensate for feedforward inaccuracies.

Policy adaptation across multiple configurations

This section describes how the control policy learned on the single honeycomb segment, with online updates, can be directly adapted to elephant-trunk robots, soft-muscle robots, hybrid-assembled robots, and worm robots, featured with distinct configurations and stiffnesses.

Policy adaptation to elephant-trunk robots. Transferring the policy to new configurations of the elephant-trunk robot does not require extensive remodelling. Only 500 motion data samples are collected under quasi-static

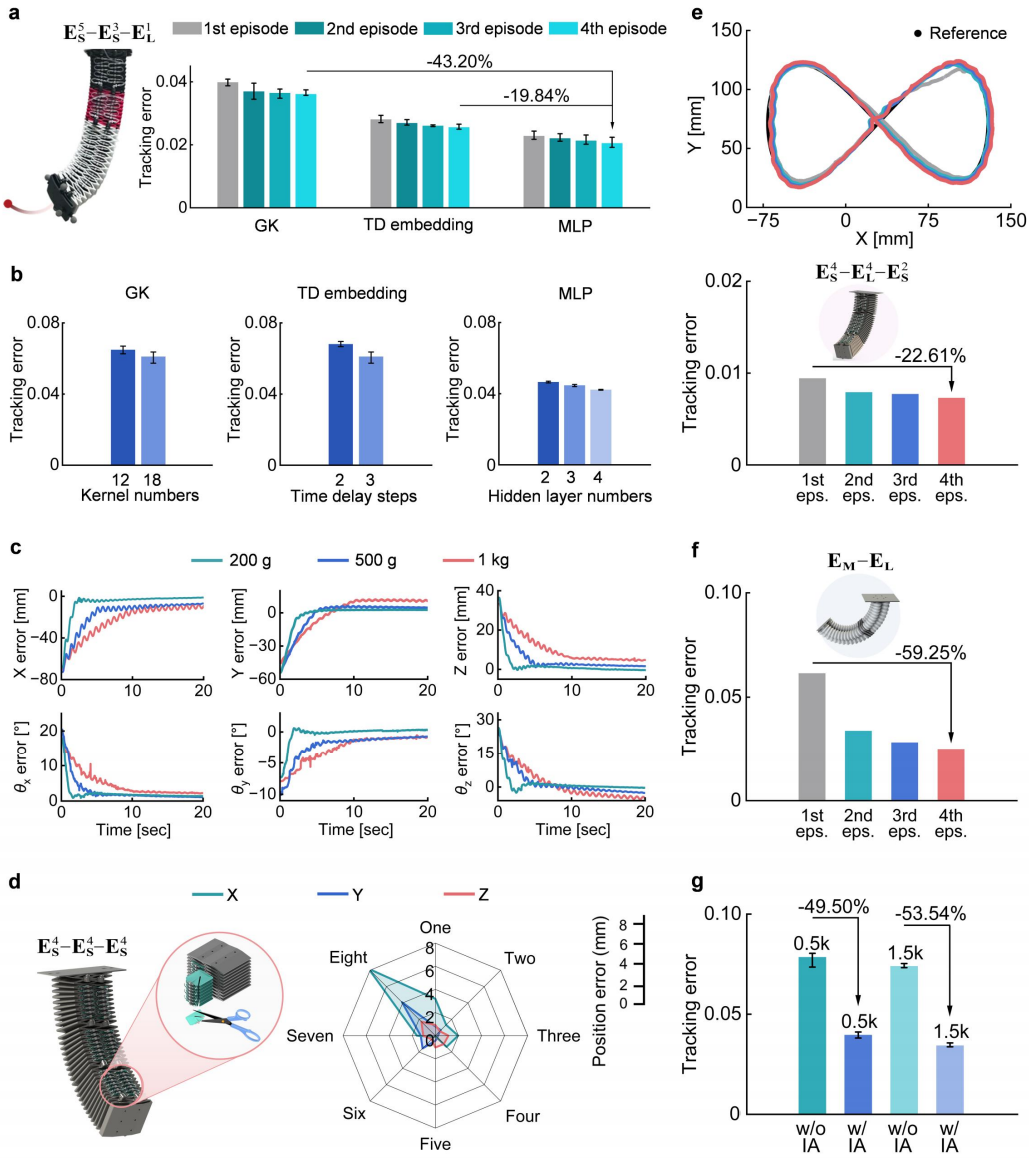

Fig. 6: **Validation of learning ability and robustness. a**, Online learning ability validation with different embeddings in target reaching of one elephant-trunk robot. **b**, Control performance under different embedding structures. **c**, Pose error curves of the robot tip under different load conditions. **d**, Empirical robustness validation under different numbers of broken airbags, Position error $:= \frac{1}{M}\sum_{i=1}^{M}\sqrt{\|p_{i,k}-p_{r,i,k}\|^2}$, $p_{i,k} = [p_{x,i,k}, p_{y,i,k}, p_{z,i,k}]^\top$ and $p_{r,i,k} = [p_{r_x,i,k}, p_{r_y,i,k}, p_{r_z,i,k}]^\top$ denote the real position and its reference at the k-th step for the i-th experiment, $M = 5$ is the number of experiments. **e**, Four-episode (eps.) learning performance in bow tie tracking of one elephant-trunk robot. **f**, Four-episode learning performance in target reaching of one worm robot. **g**, Ablation study on integral action (IA) in policy learning.

conditions to train the feedforward policy $u_r = \Phi(x_r)$ in equation (6). Here, $\Phi(\cdot)$ is a neural network with a 12-32-64-32-m architecture and Rectified ReLU activation functions (Supplementary Section 2). The feedback policy u_e in equation (9) is then refined online to adapt to new configurations in real-time.

Policy adaptation to soft-muscle and hybrid-assembled robots. Each soft-muscle segment has three control

inputs, unlike the four in the honeycomb segment. To enable policy transfer from honeycomb to soft-muscle segments, an action re-allocation strategy is designed to map the four-dimensional control space to three through geometric transformations (Supplementary Section 5). This approach allows for the direct deployment of learned policies to heterogeneous soft-muscle and hybrid-assembled robots without requiring prior modelling.

Policy adaptation to worm robots. The control policy of the elephant-trunk robot cannot be directly transferred to the worm robot, as they utilize different actuation modes (positive vs. negative pressure actuation). For policy adaptation to the worm robot, a policy initialization for u_e is employed, utilizing 10k samples to calculate the associated gain matrix K through KCID (Supplementary Section 7). Subsequently, the learned policy for the configuration E_M is transferred and updated online in the linear embedding space to accommodate other configurations of the worm robots. The effectiveness of rapid policy adaptation to heterogeneous worm robots is demonstrated in Fig. 4d. However, a key question arises: Is a newly trained Koopman embedding essential for policy transfer to heterogeneous robots? As shown in Fig. 9, policy transfer with a newly trained Koopman embedding in a worm segment (LERL-new-transfer) only slightly outperforms that using the pretrained Koopman embedding from the honeycomb segment (LERL-transfer). These results highlight that our framework enables rapid policy adaptation in heterogeneous robots without notable performance degradation.

Empirical validation

We conducted comparative studies to verify the effectiveness of our framework, including: (i) online policy learning with different embeddings; (ii) robustness validation under actuator faults and high-payloads; (iii) online multi-episode learning performance; (iv) ablation study on the integral action; and (v) fast-moving traction stick tracking.

Learning with different embeddings. We evaluated the effectiveness of our approach from two perspectives: the choice of embeddings and the ability to enhance control performance through online learning. As the embedding structure is not unique, we validate the effectiveness of LERL with embedding choices such as MLP, Gaussian kernel (GK), and time-delay (TD) embeddings. As shown in Fig. 6a, online learning reduces tracking error across all adopted embeddings as the learning episodes increase, verifying the effectiveness of online policy learning in performance improvement. The MLP-based embedding achieves the best performance, reducing the tracking error by 43.2% compared to GK and 19.84% compared to TD embedding. Furthermore, increasing the kernel numbers of GK, time delay steps of TD embedding, and the hidden layers of MLP contribute to the reduction of the tracking error (Fig. 6b).

Empirical robustness validation. The empirical robustness of LERL was validated under varying payloads and multiple actuator faults. Fig. 6c displays pose error curves (averaged over 5 trials) that further validate the robustness under different payloads, complementing the results in Fig. 4e. These curves demonstrate LERL's ability to maintain precise tracking in varying load conditions of 200 g, 500 g, and 1 kg. As shown in Fig. 6d, LERL sustains <2 mm tracking error despite seven broken airbags (Supplementary Video 6). The resilience of LERL to hardware degradation, enabled by online learning, addresses a critical barrier for field applications, where material fatigue or actuator failure is inevitable.

Online multi-episode learning. The multi-episode online learning ability of our method was validated with elephant-trunk and worm robots. Our approach enables the elephant-trunk robot in configuration E_S^4-E_L^4-E_S^2 to accurately track circular trajectories (Fig. 6e). In addition, the tracking error decreases with each learning episode (reduced by 22.61% after 4 learning episodes), verifying the online learning capability. Similarly, for the worm robot configuration E_M-E_L, the tracking error in the achievement of the target gradually reduces as the learning episode grows (reduced by 59.25% after 4 learning episodes), as shown in Fig. 6f. A visual comparison of performance before and after learning is available in Supplementary Video 7.

Ablation study on integral action. The impact of integral action (IA) on policy learning was evaluated using feedforward policies trained with 0.5 and 1.5k quasi-static motion samples. As shown in Fig. 6g, incorporating IA improves performance by 49.5% and 53.54% in the 0.5k and 1.5k sample scenarios, respectively. However, without IA, increasing feedforward policy training data from 0.5 to 1.5k yields only a marginal reduction in tracking error. These results demonstrate that IA effectively compensates for inaccurate feedforward policies and accelerates policy transfer to new configurations with limited quasi-static motion data.

Fast-moving traction stick tracking. We evaluated LERL's capability in tracking rapidly moving targets using a human-operated traction stick. The experimental results demonstrate LERL's effectiveness in controlling the tip

of an elephant-trunk soft robot (configuration E_S^5-E_L^3-E_L^1) to accurately track the fast-moving traction stick. Fig. 11 and Supplementary Video 8 illustrate the system's rapid and precise response to the stick's motion. Additional robustness tests (Supplementary Video 8) confirm LERL's ability to maintain accurate tracking while recovering promptly from external disturbances.

Data availability

All data needed to evaluate the conclusions in the paper are presented in the paper and in the Supplementary Information. Videos and source data are provided with the submission.

Code availability

The pseudocode for the Koopman embedding pretraining process and the online model-free RL algorithm is available in the GitHub repository https://github.com/xinglongzhangnudt/LERL-for-soft-robots.

References

[1] Li, G. *et al.* Self-powered soft robot in the mariana trench. *Nature* **591**, 66–71 (2021).

[2] Wang, Z., Freris, N. M. & Wei, X. Spirobs: Logarithmic spiral-shaped robots for versatile grasping across scales. *Device* (2024).

[3] Xie, Z. *et al.* Octopus-inspired sensorized soft arm for environmental interaction. *Science Robotics* **8**, 7852 (2023).

[4] Rus, D. & Tolley, M. T. Design, fabrication and control of soft robots. *Nature* **521**, 467–475 (2015).

[5] Xu, S. *et al.* Transforming machines capable of continuous 3D shape morphing and locking. *Nature Machine Intelligence* 1–13 (2025).

[6] Piqué, F. *et al.* Controlling soft robotic arms using continual learning. *IEEE Robotics and Automation Letters* **7**, 5469–5476 (2022).

[7] Haggerty, D. A. *et al.* Control of soft robots with inertial dynamics. *Science Robotics* **8**, 6864 (2023).

[8] Mamakoukas, G., Castano, M. L., Tan, X. & Murphey, T. D. Derivative-based Koopman operators for real-time control of robotic systems. *IEEE Transactions on Robotics* **37**, 2173–2192 (2021).

[9] Pan, F. *et al.* Miniature deep-sea morphable robot with multimodal locomotion. *Science Robotics* **10**, eadp7821 (2025).

[10] Yue, T. *et al.* Embodying soft robots with octopus-inspired hierarchical suction intelligence. *Science Robotics* **10**, eadr4264 (2025).

[11] Manti, M. *et al.* A bioinspired soft robotic gripper for adaptable and effective grasping. *Soft Robotics* **2**, 107–116 (2015).

[12] Ren, Z. & Sitti, M. Design and build of small-scale magnetic soft-bodied robots with multimodal locomotion. *Nature Protocols* **19**, 441–486 (2024).

[13] Kim, S., Laschi, C. & Trimmer, B. Soft robotics: a bioinspired evolution in robotics. *Trends in Biotechnology* **31**, 287–294 (2013).

[14] Shah, D. S. *et al.* A soft robot that adapts to environments through shape change. *Nature Machine Intelligence* **3**, 51–59 (2021).

[15] Mo, H. *et al.* Data-efficient learning control of continuum robots in constrained environments. *IEEE Transactions on Automation Science and Engineering* (2024).

[16] Freeman, C., Maynard, M. & Vikas, V. Topology and morphology design of spherically reconfigurable homogeneous modular soft robots. *Soft Robotics* **10**, 52–65 (2023).

[17] Li, S. *et al.* Scaling up soft robotics: A meter-scale, modular, and reconfigurable soft robotic system. *Soft Robotics* **9**, 324–336 (2022).

[18] Milana, E., Santina, C. D., Gorissen, B. & Rothemund, P. Physical control: A new avenue to achieve intelligence in soft robotics. *Science Robotics* **10**, eadw7660 (2025).

[19] Liu, J. *et al.* Data-driven methods for sensing, modeling and control of soft continuum robot: A review. *IEEE/ASME Transactions on Mechatronics* 1–11 (2025).

[20] Armanini, C., Boyer, F., Mathew, A. T., Duriez, C. & Renda, F. Soft robots modeling: A structured overview. *IEEE Transactions on Robotics* **39**, 1728–1748 (2023).

[21] Renda, F., Boyer, F., Dias, J. & Seneviratne, L. Discrete cosserat approach for multisection soft manipulator dynamics. *IEEE Transactions on Robotics* **34**, 1518–1533 (2018).

[22] Till, J., Aloi, V. & Rucker, C. Real-time dynamics of soft and continuum robots based on cosserat rod models. *The International Journal of Robotics Research* **38**, 723–746 (2019).

[23] Huang, X., Rong, Y. & Gu, G. High-precision dynamic control of soft robots with the physics-learning hybrid modeling approach. *IEEE/ASME Transactions on Mechatronics* (2024).

[24] Braganza, D., Dawson, D. M., Walker, I. D. & Nath, N. A neural network controller for continuum robots. *IEEE Transactions on Robotics* **23**, 1270–1277 (2007).

[25] Giorelli, M. *et al.* Neural network and Jacobian method for solving the inverse statics of a cable-driven soft arm with nonconstant curvature. *IEEE Transactions on Robotics* **31**, 823–834 (2015).

[26] Kim, D., Park, M. & Park, Y.-L. Probabilistic modeling and bayesian filtering for improved state estimation for soft robots. *IEEE Transactions on Robotics* **37**, 1728–1741 (2021).

[27] Korda, M. & Mezić, I. Linear predictors for nonlinear dynamical systems: Koopman operator meets model predictive control. *Automatica* **93**, 149–160 (2018).

[28] Mamakoukas, G., Abraham, I. & Murphey, T. D. Learning stable models for prediction and control. *IEEE Transactions on Robotics* **39**, 2255–2275 (2023).

[29] Zhang, X., Pan, W., Scattolini, R., Yu, S. & Xu, X. Robust tube-based model predictive control with Koopman operators. *Automatica* **137**, 110114 (2022).

[30] Bruder, D., Fu, X., Gillespie, R. B., Remy, C. D. & Vasudevan, R. Koopman-based control of a soft continuum manipulator under variable loading conditions. *IEEE Robotics and Automation Letters* **6**, 6852–6859 (2021).

[31] Bruder, D., Fu, X., Gillespie, R. B., Remy, C. D. & Vasudevan, R. Data-driven control of soft robots using Koopman operator theory. *IEEE Transactions on Robotics* **37**, 948–961 (2020).

[32] Pan, J. *et al.* Auto-generation of mission-oriented robot controllers using bayesian-based Koopman operator. *IEEE Transactions on Robotics* (2023).

[33] Wang, J. *et al.* An improved Koopman-MPC framework for data-driven modeling and control of soft actuators. *IEEE Robotics and Automation Letters* **8**, 616–623 (2022).

[34] Kober, J., Bagnell, J. A. & Peters, J. Reinforcement learning in robotics: A survey. *The International Journal of Robotics Research* **32**, 1238–1274 (2013).

[35] Meng, Y. *et al.* Preserving and combining knowledge in robotic lifelong reinforcement learning. *Nature Machine Intelligence* **7**, 256–269 (2025).

[36] Medany, M., Piglia, L., Achenbach, L., Mukkavilli, S. K. & Ahmed, D. Model-based reinforcement learning for ultrasound-driven autonomous microrobots. *Nature Machine Intelligence* 1–15 (2025).

[37] Han, L. *et al.* Lifelike agility and play in quadrupedal robots using reinforcement learning and generative pre-trained models. *Nature Machine Intelligence* **6**, 787–798 (2024).

[38] Naughton, N. *et al.* Elastica: A compliant mechanics environment for soft robotic control. *IEEE Robotics and Automation Letters* **6**, 3389–3396 (2021).

[39] Bing, Z., Yun, Y., Huang, K. & Knoll, A. Context-based meta-reinforcement learning with bayesian nonparametric models. *IEEE Transactions on Pattern Analysis and Machine Intelligence* **46**, 6948–6965 (2024).

[40] Thuruthel, T. G., Falotico, E., Renda, F. & Laschi, C. Model-based reinforcement learning for closed-loop dynamic control of soft robotic manipulators. *IEEE Transactions on Robotics* **35**, 124–134 (2018).

[41] Satheeshbabu, S., Uppalapati, N. K., Fu, T. & Krishnan, G. Continuous control of a soft continuum arm using deep reinforcement learning. *2020 3rd IEEE International Conference on Soft Robotics (RoboSoft),* 497–503 (2020).

[42] Nazeer, M. S., Laschi, C. & Falotico, E. RL-based adaptive controller for high precision reaching in a soft robot arm. *IEEE Transactions on Robotics* (2024).

[43] Centurelli, A. *et al.* Closed-loop dynamic control of a soft manipulator using deep reinforcement learning. *IEEE Robotics and Automation Letters* **7**, 4741–4748 (2022).

[44] Jiang, H. *et al.* Hierarchical control of soft manipulators towards unstructured interactions. *The International Journal of Robotics Research* **40**, 411–434 (2021).

[45] Gupta, A., Savarese, S., Ganguli, S. & Fei-Fei, L. Embodied intelligence via learning and evolution. *Nature Communications* **12**, 5721 (2021).

[46] Wang, D. *et al.* Dexterous electrical-driven soft robots with reconfigurable chiral-lattice foot design. *Nature Communications* **14**, 5067 (2023).

[47] Proctor, J. L., Brunton, S. L. & Kutz, J. N. Generalizing Koopman theory to allow for inputs and control. *SIAM Journal on Applied Dynamical Systems* **17**, 909–930 (2018).

[48] Korda, M. & Mezić, I. On convergence of extended dynamic mode decomposition to the Koopman operator. *Journal of Nonlinear Science* **28**, 687–710 (2018).

[49] Formentin, S. & Chiuso, A. Control-oriented regularization for linear system identification. *Automatica* **127**, 109539 (2021).

[50] Lancaster, P. & Rodman, L. Algebraic Riccati equations. *Clarendon press* (1995).

Competing interests The authors declare that they have no competing interests.

Additional information
Supplementary information The supplementary material is attached with the submission.
Correspondence and requests for materials should be addressed to Xinglong Zhang, Xin Xu, Dewen Hu.

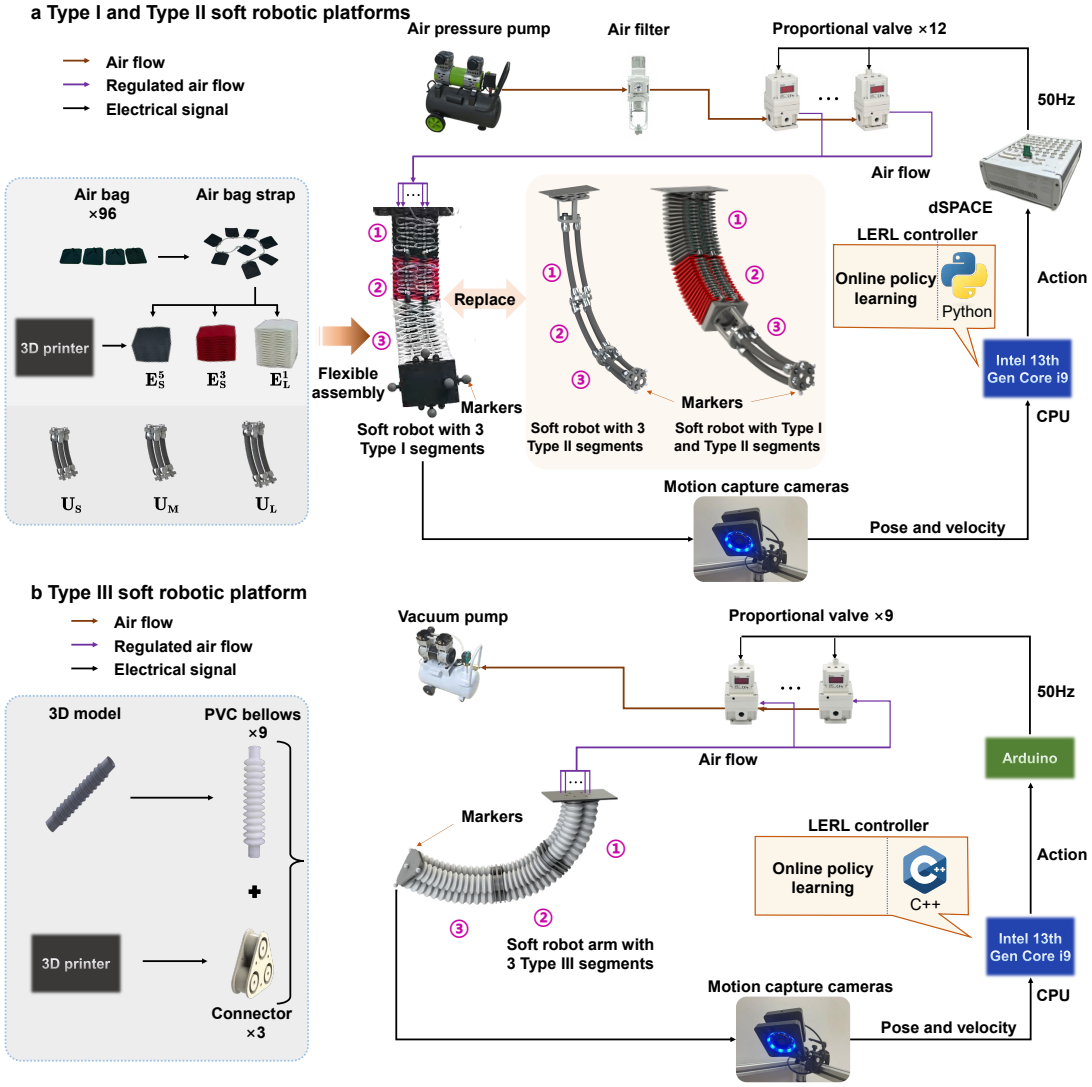

Fig. 7: **a**, Type I and Type II soft robotic platforms in specific configurations. Two types of robots share the same motion capture module and the computing unit but with different pneumatic actuation systems across different configurations. **b**, Type III soft robotic platform in a particular setup. Three soft robotic platforms, with their multiple configurations (including hybrid-assembled configurations), can perform various tasks.

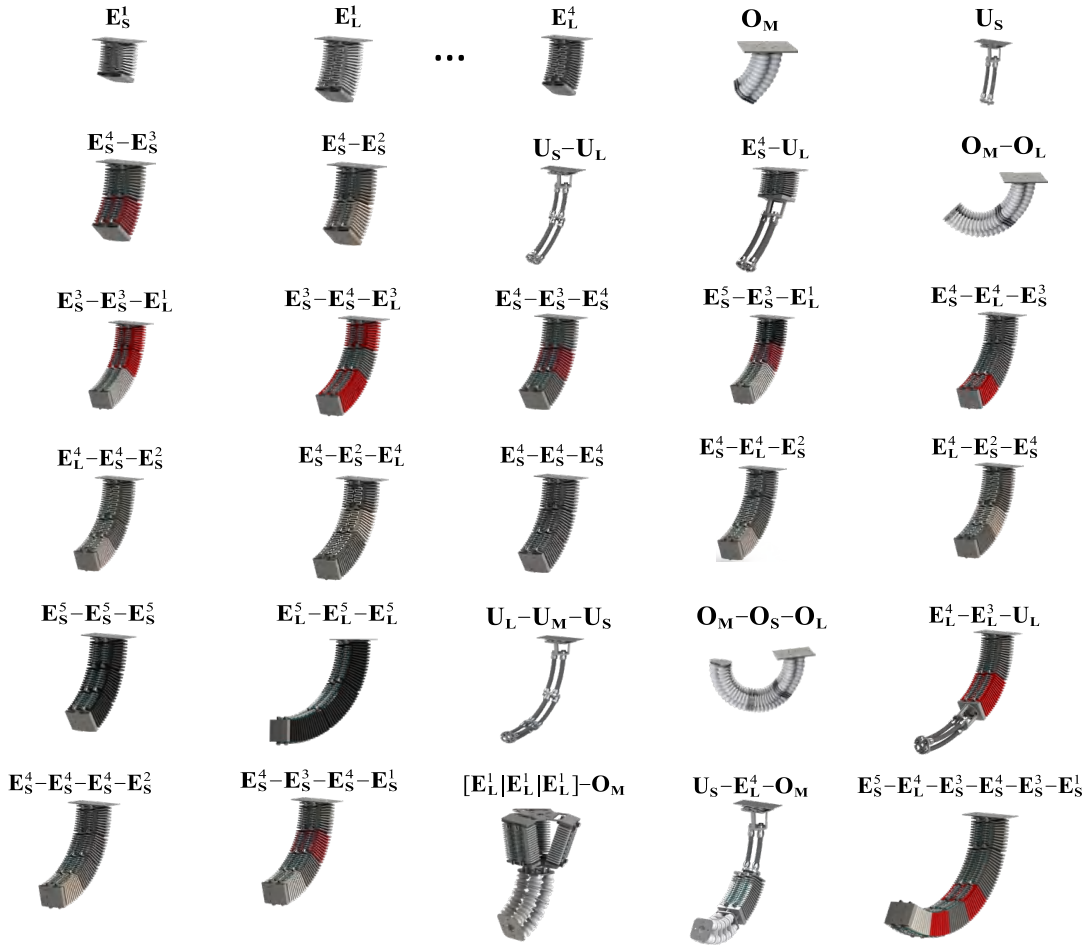

Fig. 8: **List of 30 configurations of soft robots for validation.** A library of modular segments includes eight honeycomb segments (E_S^1, E_S^2, E_S^3, E_S^4, E_L^1, E_L^2, E_L^3, E_L^4), three soft-muscle segments (E_S, E_M, E_L) and three worm segments (E_S, E_M, E_L), varying in length and stiffness. These segments are assembled to build 22 configurations of elephant-trunk robots that vary in segment length, stiffness, quantity, and assembly orders; three configurations of soft-muscle robots and two configurations of hybrid-assembled robots; and three configurations of worm robots ranging from one to three segments.

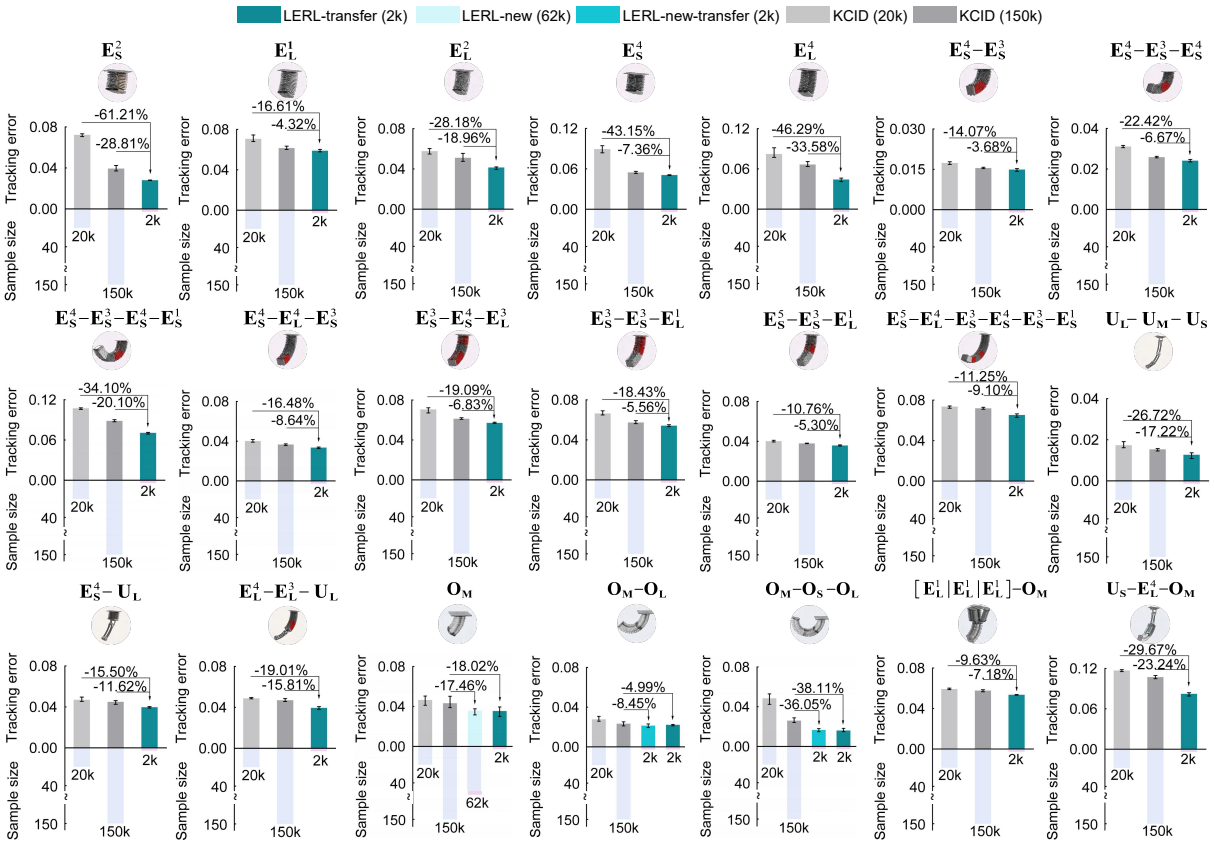

Fig. 9: **Auxiliary policy adaptation performance across diverse configurations in target reaching tasks.** Target reaching performance comparisons across 18 configurations from three soft robot prototypes demonstrate that LERL outperforms KCID in both tracking error and sample size reduction, Tracking error $:= \frac{1}{M \cdot N} \sum_{i=1}^{M} \sum_{k=1}^{N} \left\| \bar{x}_{i,k} - \bar{x}_{r,i,k} \right\|^2$, $\bar{x}_{i,k}, \bar{x}_{r,i,k} \in \mathbb{R}^{12}$ represent the normalized real state variable (pose and velocity) and its reference at the k-th step for the i-th experiment, N denotes the algorithm horizon, and $M = 5$ is the number of repeated experiments. The policy adaptation to worm robots' configurations uses policy learning with a newly trained Koopman embedding (LERL-new). The Koopman embedding for the single worm segment $\mathrm{E_M}$ is trained with 20k samples, and the policy is updated online from scratch using 2k samples. The policy is then transferred and refined online (LERL-new-transfer) to different configurations with 2k samples under the newly trained Koopman embedding.

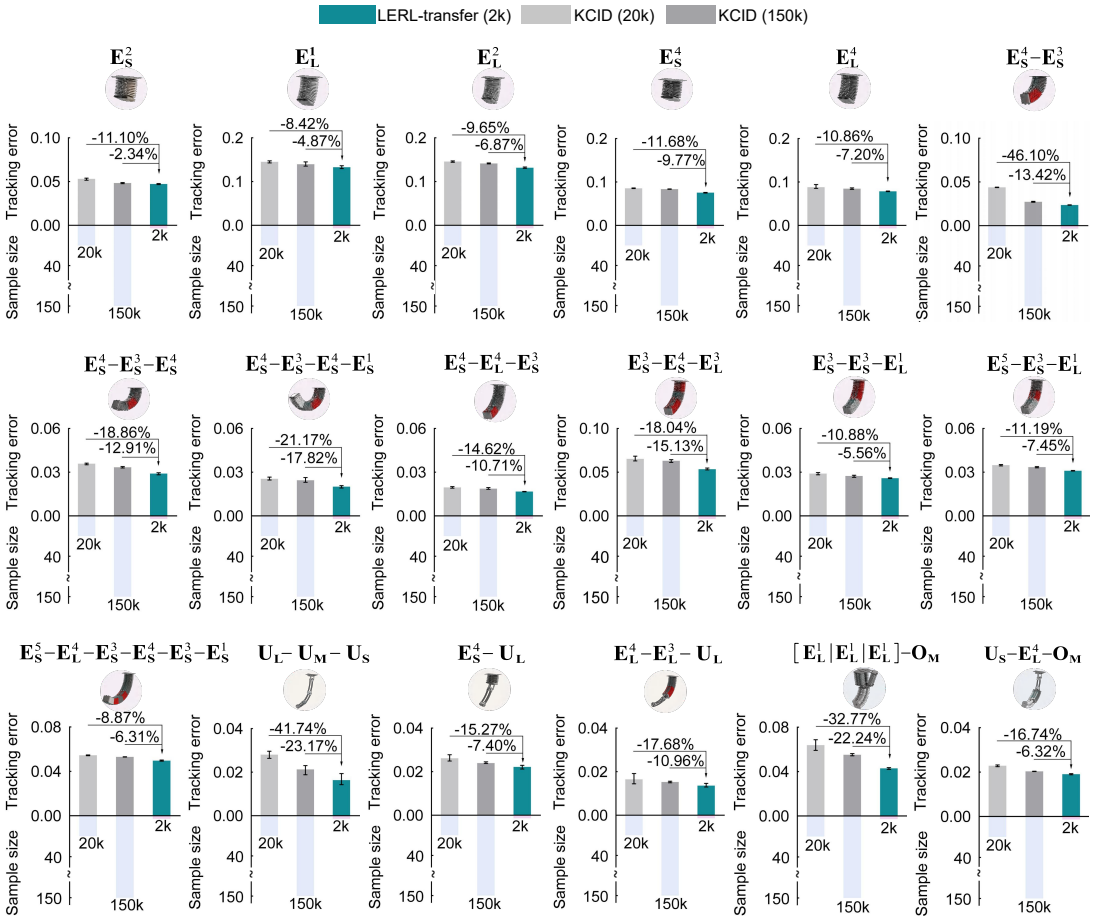

Fig. 10: **Auxiliary policy adaptation performance across diverse configurations in bow tie tracking tasks.** Bow tie tracking performance comparisons across 15 configurations from three soft robot prototypes demonstrate that LERL outperforms KCID in both tracking error and sample size reduction.

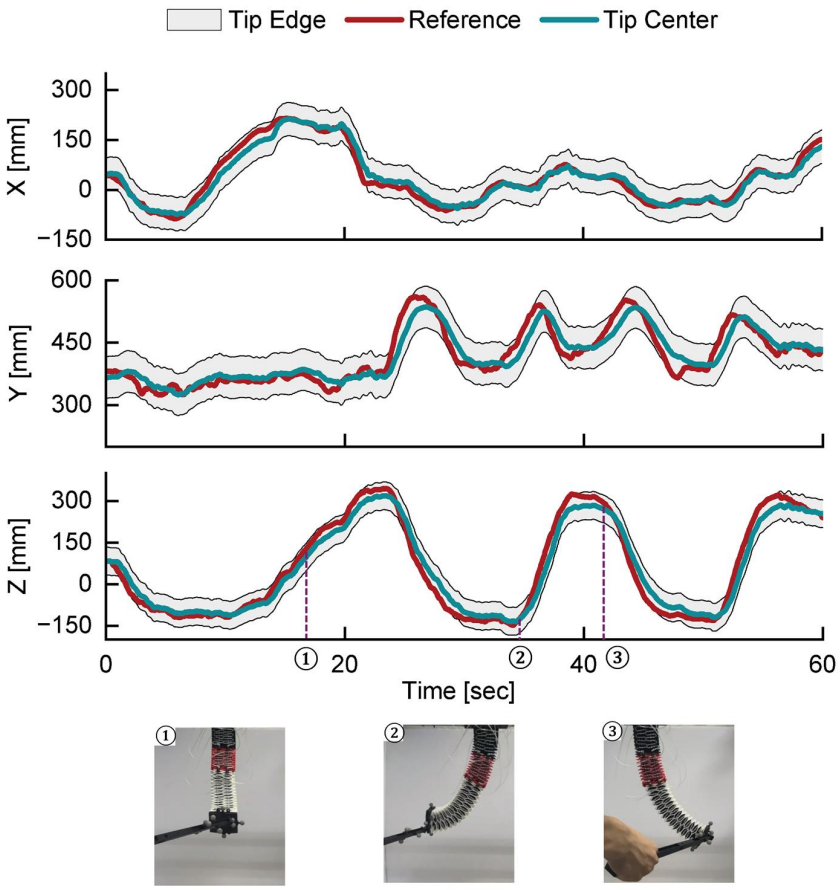

Fig. 11: **Fast-moving traction stick tracking performance.** Tracking curves in the x, y, and z directions, along with the pose of the soft robot at selected moments.

Table 2: Computational (comp.) time per step on the Type I elephant-trunk robots. The computation is conducted on a laptop equipped with a 13th Gen Intel (R) Core (TM) i9-13900HX processor, featuring a base clock speed of 2.20 GHz.

Robot configuration	**Input dimension**	**Lifted space dimension**	**Average comp. time (ms)**	**Max comp. time (ms)**
One segment	4	24	1.862	4.004
Two segments	8	24	2.429	5.001
Three segments	12	24	3.508	8.001
Four segments	16	24	3.831	8.998

Supplementary Information

Reinforcement learning in linear embedding space unlocks generalizable control across soft robot configurations

Supplementary information contains:

Supplementary Section 1. Koopman embedding training
Supplementary Section 2. Feedforward policy calculation
Supplementary Section 3. Policy learning with warm-start
Supplementary Section 4. Pseudocode of LERL
Supplementary Section 5. Action space re-allocation
Supplementary Section 6. Policy adaptation to rigid-body robots
Supplementary Section 7. Feedback policy initialization
Supplementary Section 8. Theoretical results
Supplementary Table 1. Hyperparameters
Supplementary Video 1. Hammering nails task
Supplementary Video 2. Serving drinks with safe interactions
Supplementary Video 3. Calligraphy brush handwriting
Supplementary Video 4. Quick hand-eye reaction game
Supplementary Video 5. Policy adaptation performance validation
Supplementary Video 6. Empirical robustness validation
Supplementary Video 7. Performance improvement from online learning
Supplementary Video 8. Fast-moving traction stick tracking

Supplementary Section 1. Koopman embedding training

The 20k collected samples are used to train the Koopman embedding on a laptop with an NVIDIA GeForce RTX 4090 GPU. Hyperparameters for offline Koopman embedding training are provided in Supplementary Table 1.

The regression loss L_e is the mean squared error between the lifted actual and predicted states over p steps, which measures the prediction accuracy in the embedding space, i.e.,

$$L_e = \frac{1}{p}\sum_{i=1}^{p} \|s_{k+i} - \hat{s}_{k+i}\|^2, \tag{S1}$$

where $\hat{s}_{k+i} = A^i s_k + \sum_{j=1}^{i} A^{j-1} B u_{k+i-j}$ is the i-th step ahead state prediction in the linear embedding space from time instant k.

The reconstruction loss L_r is the mean squared error between the actual states and their predicted reconstructed counterparts over p steps, that is,

$$L_r = \frac{1}{p}\sum_{i=1}^{p} \|x_{k+i} - \hat{x}_{k+i}\|^2, \tag{S2}$$

where the $\hat{x}_{k+i} = T^{-1} s_{k+i}$ is the prediction of the reconstruction state.

To guarantee the matrix T in equation (S2) to be invertible, we parameterize T as a trainable tensor and introduce the following regularization loss:

$$L_T = \sum_{i=1}^{12} \|\lambda(T)_i - 1\|^2, \tag{S3}$$

to shape its eigenvalues near the unit circle.

Supplementary Section 2. Feedforward policy calculation

A feedforward policy u_r is incorporated into the control strategy (equation (6) in Methods) to maintain the robot tip in the desired pose when the dynamic feedback policy $u_e = Ks_e$ vanishes. However, this static feedforward policy is not directly available, as the robot tip's static model is unknown. We address this challenge by learning the feedforward policy offline using precollected quasi-static motion data[7]. The embedding network, an MLP with an architecture of 12-32-64-32-m and Rectified Linear Unit (ReLU) activation functions, is adopted to generate u_r. Here, m denotes the input dimension of the current robot configuration, determined by the robot type and the number of segments. The Adam optimizer is adopted to train the network parameters offline, using $N_f = 500$ quasi-static motion samples of $\{u_r, x_r\}$ to minimize the following mean squared error:

$$E_r = \frac{1}{N_f} \sum_{i=1}^{N_f} \|u_{r,i} - \Phi(x_{r,i})\|^2. \tag{S4}$$

The resulting feedforward policy for each robot configuration is represented as $u_r = \Phi(x_r)$, where $\Phi(\cdot)$ is the pretrained MLP tailored for each robot configuration.

Supplementary Section 3. Policy learning with warm-start

Here we present the implementation of policy learning with warm-start to further enhance learning efficiency. Even in scenarios with nonlinear system dynamics, a stabilizing control policy can still be effectively derived. In this work, a straightforward way is to carry out a model-based control design using offline learned Koopman models, which makes full use of the baseline control policy $u_{e,b}$ and the associated H_b matrix.

Let $\Delta H_i = H_b - \hat{H}_i$, equation (10) in Methods is equivalent to solving:

$$\min_{\Delta h_{i+1}} \|\Delta h_{i+1}^\top z_k - \Delta d(z_k, \Delta H_i)\|^2, \tag{S5}$$

where $\Delta d(z_k, \Delta H_i) = h_b^\top z_k - d(z_k, \hat{H}_i)$.

Then, we derive the update for Δh_{i+1} as

$$\Delta h_{i+1} = (ZZ^\top)^{-1} Z \Delta W, \tag{S6}$$

where $\Delta W = [\Delta d(z_{[1]}, \Delta h_i) \cdots \Delta d(z_{[N]}, \Delta h_i)]^\top$.

Remark 1 *Note that the baseline control policy $u_{e,b}$ is not necessarily computed from a model-based controller design. The associated matrix H_b could be estimated by recursively solving equation (10) with an available control policy $u_{e,b}$.*

Let a lower bound of the computational residual error of h_i be $\epsilon_{h,i}$. The following proposition states the advantage of equation (S6) over equation (11) in numerical precision.

Proposition 1 (Numerical precision error) *If H_b is such that $\Delta H_i \succ 0$ and there exists $\delta > 1$ with $\delta \Delta d \leq d$, then the numerical precision error of h_i with the operation in equation (S6) is smaller than $\delta^{-1}\epsilon_{h,i}$.*

Proof. Note that the numerical computational error is due to the inverse operation and the weak fulfillment of $ZZ^\top$ being full rank. Let the error in operation $(ZZ^\top)^{-1}$ associated with the i-th iteration be $\epsilon_{z,i}$. Then, we have $\epsilon_{h,i+1} = \epsilon_{z,i} ZW$. Similarly, the numerical error of Δh_{i+1} is $\epsilon_{\Delta h,i+1} = \epsilon_{z,i} Z \Delta W$. In view of the fact $\delta \Delta d \leq d$ and the definition of W and ΔW, we have $\epsilon_{\Delta h,i+1} \leq \epsilon_{z,i} Z \delta^{-1} W = \delta^{-1} \epsilon_{h,i}$. Note that $\hat{H}_i = \Delta H_i + H_b$, hence the computation of the vectorization of $\hat{H}_i$ using the operation in equation (S6) results in a numerical precision error smaller than $\delta^{-1}\epsilon_{h,i}$. □

Supplementary Section 4. Pseudocode of LERL

The main implementation steps of linear embedding RL (LERL) for policy learning across diverse configurations are outlined in Algorithm 1. These steps include offline Koopman embedding pretraining and online policy learning. The offline phase establishes baseline capabilities, while the online phase allows adaptive refinement for improved performance. The online update of h can follow three strategies: (a) least-square (LS) rule: update h using equation (11); (b) LS rule with warm-start: update Δh using equation (S6) and set $h = h_b - \Delta h$; (c) gradient-descent rule: update h using the Adam optimizer.

Supplementary Algorithm 1 Pseudocode of LERL for multiple configurations

Offline design on single honeycomb segment:

Collect open-loop input-state data;
Construct $\Psi(x)$ with equation (2) using an MLP;
Offline train the Koopman embedding with the loss in equation (5);
Offline train the feedforward policy using equation (S4);

Offline design for new configurations:

Collect 500 input-state samples in the quasi-static condition;
Offline train the feedforward policy for each new configuration using equation (S4);

Online policy learning for diverse configurations:

Require: $i = 0, N_{\max}, \{x_r\}$.

Determine the input dimension m of the current robot configuration;
Initialize u_e and $\hat{H}$ with those from the transferred policy;
while $i \leq N_{\max}$ **do**
    Measure state x_i, generate s_r and s_i using the pretrained Koopman embedding;
    Generate the feedforward policy $u_r = \Phi(s_r)$ for the current configuration;
    Calculate $u_{e,i} = -\hat{H}_{uu,i}^{-1}\hat{H}_{us,i}s_{e,i} + n_{e,i}$, in which $n_{e,i}$ is applied in initial several steps;
    Apply $u_i = u_{e,i} + u_r$ to the robot and calculate $d(z_i, \hat{H}_i) = l(z_i) + \gamma\|z_i^+\|^2_{\hat{H}_i}$;
    Update h_{i+1}; // Choose strategy (c) (Adam optimizer) with limited data, or strategies (a) and (b) (LS rule and LS rule with warm-start) when sufficient data is available.
    Construct $\hat{H}_{i+1}$ with h_{i+1};
    Set $i = i + 1$;
end while

Supplementary Section 5. Action space re-allocation

Policy transfer to elephant-trunk soft robots. We adopt the padding procedure to transfer the feedback policy $u_e = Ks_e = K(\Psi(x) - \Psi(x_d))$, $K \in \mathbb{R}^{4\times 24}$, trained on the honeycomb segment $\mathrm{E}^1_{\mathrm{S}}$, to elephant-trunk soft robots in multiple configurations. For a configuration with n segments, we transfer the policy gain K by replicating it n times, forming $K_{n,0} = [K; \cdots; K] \in \mathbb{R}^{4n\times 24}$. The policy gain $K_{n,0}$ then initializes the policy learning process for the new configuration and is fine-tuned online.

Policy transfer to soft-muscle robots. Each elephant-trunk segment has four control inputs, while the soft-muscle segment has three. To allow direct policy transfer from the elephant-trunk robot to the soft-muscle robot, we use an action re-allocation strategy. In particular, we first represent the transferred policy from the elephant-trunk robot as a virtual control policy $\bar{u} \in \mathbb{R}^4$ for the soft-muscle robot, which is then mapped to three channels using:

$$u = T_a \cdot \bar{u}, \tag{S7}$$

where the action distribution matrix $T_a \in \mathbb{R}^{3\times 4}$ is derived from equation (S8) to equation (S10).

The above re-allocation strategy allows directly transferring the control policy from the elephant-trunk robot to the soft-muscle and hybrid-assembled robots, without any prior modelling procedure.

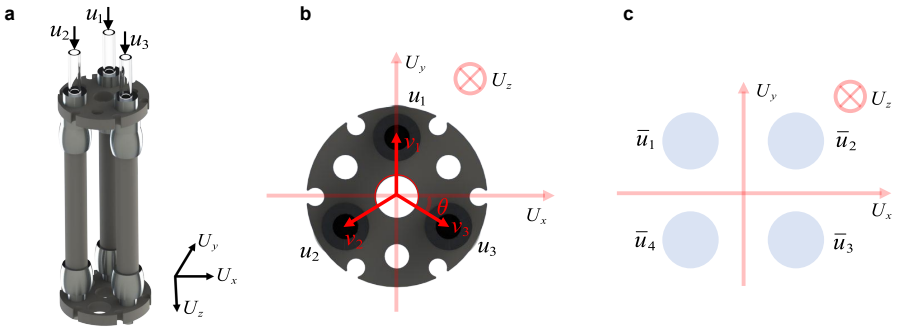

Supplementary Fig. 1: **Mechanism of the action re-allocation strategy. a**, Illustration of the equivalent actuation U of a soft-muscle segment. **b**, Illustration of the intermediate variable v, $\theta = \pi/6$. **c**, Illustration of the virtual control $\bar{u}$.

Calculation of matrix T_a. The soft-muscle segment has two bending degrees of freedom (DoF) and one elongation DoF, represented by the introduced equivalent actuation $U = [U_x, U_y, U_z]^\top$ (Supplementary Fig. 1a). Using the virtual variable $v = [v_1, v_2, v_3]^\top$ as a bridge (Supplementary Fig. 1b), the following matrix T_{a_1} is computed to map the real actuation $u = [u_1, u_2, u_3]^\top$ to the equivalent actuation U, i.e.,

$$\begin{bmatrix} U_x \\ U_y \\ U_z \end{bmatrix} = \underbrace{\begin{bmatrix} 0 & 3\sqrt{3}/4 & -3\sqrt{3}/4 \\ -3/2 & 3/4 & 3/4 \\ 1/3 & 1/3 & 1/3 \end{bmatrix}}_{T_{a_1}} \begin{bmatrix} u_1 \\ u_2 \\ u_3 \end{bmatrix}. \tag{S8}$$

The virtual actuation $\bar{u} = [\bar{u}_1, \bar{u}_2, \bar{u}_3, \bar{u}_4]^\top$ (Supplementary Fig. 1c) is mapped to the equivalent actuation U through a matrix T_{a_2}, i.e.,

$$\begin{bmatrix} U_x \\ U_y \\ U_z \end{bmatrix} = \underbrace{\begin{bmatrix} 1 & 1 & -1 & -1 \\ -1 & -1 & 1 & 1 \\ 1 & 1 & 1 & 1 \end{bmatrix}}_{T_{a_2}} \begin{bmatrix} \bar{u}_1 \\ \bar{u}_2 \\ \bar{u}_3 \\ \bar{u}_4 \end{bmatrix}. \tag{S9}$$

Combing equation (S8) with equation (S9), one has

$$T_a = T_{a_1}^{-1} T_{a_2}. \tag{S10}$$

Supplementary Section 6. Policy adaptation to rigid-body robots

To further validate the versatility of our LERL framework, we transfer the policy learned on the soft robotic segment E_S^1 to a three-segment rigid-body robot for a target reaching task. The rigid-body robot is designed in the Mujoco environment (Supplementary Fig. 2), with each segment actuated by the virtual force $u_{\text{rig}} = [u_x, u_y]^\top \in \mathbb{R}^2$ on the plane vertical to the rigid body. The controlled states, i.e., robot tip's pose and velocity, remain consistent with those in the soft robot scenario. We use the action allocation strategy introduced in Supplementary Section 5 to transfer the policy $u \in \mathbb{R}^4$ learned on the honeycomb segment to each segment of the rigid-body robot, i.e.,

$$u_{\text{rig}} = \begin{bmatrix} -1/2 & -1/2 & 1/2 & 1/2 \\ 1/2 & -1/2 & -1/2 & 1/2 \end{bmatrix} u. \tag{S11}$$

As shown in Supplementary Fig. 2, directly transferring the policy via the control action re-allocation strategy in equation (S11) leads to instability in the target-reaching task. This is because the virtual forces in the rigid-body robot differ in physical interpretation from the air voltage inputs in the honeycomb segment. However, online policy learning via model-free RL in the shared Koopman embedding space, pretrained on the honeycomb segment E_S^1, enables rapid convergence to the target. This demonstrates the effectiveness of our LERL framework in fast adaptation to rigid-body robots. Future work will explore its applicability across various real-world rigid-body robotic systems.

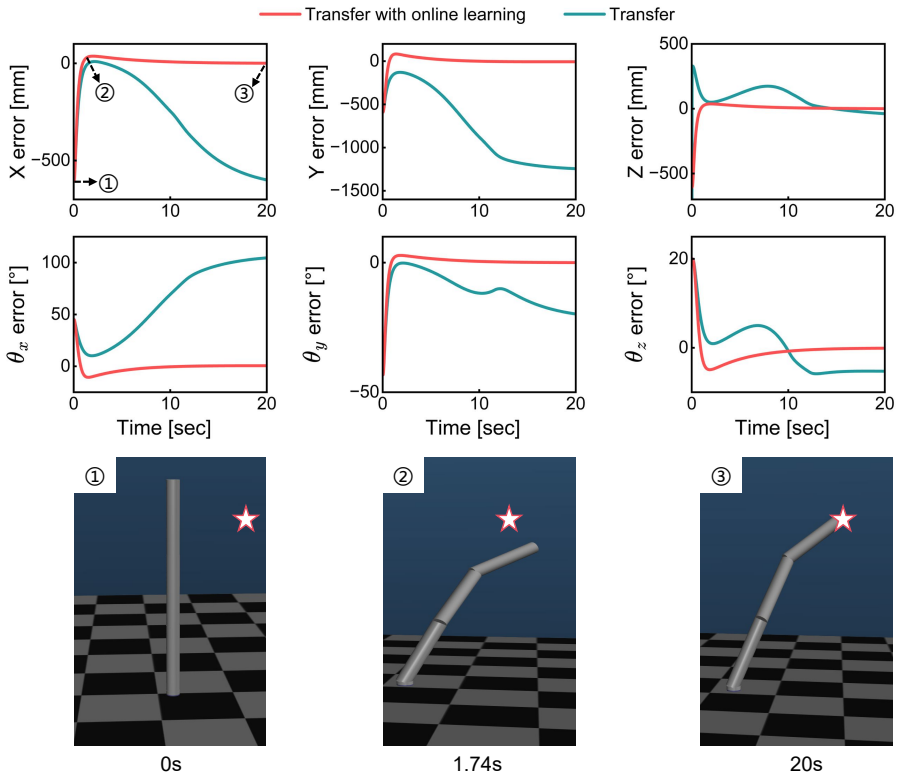

Supplementary Fig. 2: **Policy adaptation to rigid robots.** Pose error curves for policy transfer with or without online learning scenarios, along with the pose of the rigid-body robot at selected moments. The highlighted star is the reference target of the robot tip.

Supplementary Section 7. Feedback policy initialization

The elephant-trunk robot and the worm robot utilize different actuation modes: positive and negative pressure actuation, respectively. Thereby, a significant gap arises between these heterogeneous robots within the same pretrained Koopman embedding when transferring the policy trained on the honeycomb segment to the worm robots.

To bridge the aforementioned gap, we effortlessly initialize the feedback policy u_e using just 10k samples $\{x, u\}$ via KCID[7]. Specifically, given the pretrained Koopman embedding $\Psi(\cdot)$ from the honeycomb segment, the model parameters A and B are first calculated via solving:

$$\min_{A,B} \sum_{i=1}^{N_0} \|s_{i+1} - As_i - Bu_i\|^2, \tag{S12}$$

where $s_{i+1} = \Psi(x_{i+1})$ and $s_i = \Psi(x_i)$, $N_0 = 10k$.

Using the calculated A and B, an initialized feedback policy $u_e = K_0 s_e$ is generated by solving the standard LQR problem:

$$\begin{aligned} \min_{u_e} & \sum_{k=0}^{+\infty} s_{e,k}^\top Q_0 s_{e,k} + u_{e,k}^\top R_0 u_{e,k}, \\ \text{s.t.} \;\; & s_{e,k+1} = As_{e,k} + Bu_{e,k}, \end{aligned} \tag{S13}$$

where $Q_0 \in \mathbb{R}^{n_\psi \times n_\psi}$ and $R_0^{m \times m}$ are chosen as positive-definite matrices.

Supplementary Section 8. Theoretical results

This section theoretically demonstrates that, under mild assumptions, LERL with the least-square update rule (11) outperforms a robust KCID that accounts for modelling errors.

Assume that the reference pair $\{x_r, u_r\}$ is reachable, i.e., $x_r = f(x_r, u_r)$, where $f(\cdot,\cdot)$ is the unknown dynamics of the soft robot. The dynamic model of the state error is described as $x_e^+ = f_e(x_e, u_e) := f(x,u) - f(x_r, u_r)$. The resulting error dynamics on the embedding space is given as

$$s_e^+ = As_e + Bu_e + w_e(s_e, u_e). \tag{S14}$$

According to optimal control theory, a stabilizing feedback policy $u_e = Ks_e$ results in a quadratic value function $V(s_e) = s_e^\top P s_e$ when $w_e(s_e, u_e) = 0$ holds, where $P \in \mathbb{R}^{n_\psi \times n_\psi}$ is a symmetric positive definite matrix. However, since $w_e(s_e, u_e)$ is non-negligible, the feedback policy u_e, applied to the model in equation (1), leads to a time-dependent value function $V(s_{e,k}) = s_{e,k}^\top P_k s_{e,k}$, where P_k varies with time. Hence, the so-called Q-function (state-action value function), i.e., $Q(z_k) := l(z_k) + \gamma V(As_{e,k} + Bu_{e,k} + w_{e,k})$, can be rewritten as

$$Q(z_k) = z_k^\top H_o z_k + G(z_k) := z_k^\top H(P_k) z_k, \tag{S15}$$

where $z_k := [s_{e,k}^\top,\ u_{e,k}^\top]^\top$; $H_o = \begin{bmatrix} Q + \gamma A^\top P_k A & \gamma A^\top P_k B \\ \gamma B^\top P_k A & R + \gamma B^\top P_k B \end{bmatrix}$; $H(P_k) = \begin{bmatrix} H_{ss}(P_k) & H_{su}(P_k) \\ H_{us}(P_k) & H_{uu}(P_k) \end{bmatrix}$ is a matrix on P_k, expressed in a block form similar to H_o; the term $G(z_k)$ originates from the modelling error. Since it is directly tied to the input-state pair, we leverage $G(z_k)$ to enhance control performance, rather than treating it as an uncertainty that degrades performance[29].

To prove the theoretical property, we introduce the following assumptions about the equivalent Koopman error model in equation (S14).

Lemma 1 (Equivalent Koopman error model[29])
(a) Model (S14) is stabilizable at $s_e = 0$ if and only if $f_e(x_e, u_e)$ is stabilizable.
(b) The model uncertainty $w_e(s_e, u_e) = \Psi(f(\Psi^{-1}(s_e), u_e)) - As_e - Bu_e$ satisfies:

$$\|w_e(s_e, u_e)\|^2 \le L_s \|s_e\|^2 + L_u \|u_e\|^2, \tag{S16}$$

where L_s and L_u are bounded constants.

Assumption 1 *There exists an $\epsilon > 0$ such that the following Lyapunov equation has a solution on $\bar{P} \in \mathbb{R}^{n_\psi \times n_\psi}$ and $\bar{K} \in \mathbb{R}^{m \times n_\psi}$, i.e.,*

$$\bar{P} = \tilde{Q} + \bar{K}^\top \tilde{R} \bar{K} + \gamma F^\top \tilde{P} F, \tag{S17}$$

where $\tilde{P} = \bar{P} + \epsilon \bar{P}^2$, $\tilde{Q} = Q + \gamma(1+\epsilon)/\epsilon L_s$, $\tilde{R} = R + \gamma(1+\epsilon)/\epsilon L_u$.

Remark 2 *An optimal solution can be calculated by setting $\partial \bar{P} / \partial K = 0$, which leads to:*

$$\bar{K} = -\gamma T(\bar{P})^{-1} B^\top \tilde{P} A, \tag{S18}$$

where $T(P) = \tilde{R} + \gamma B^\top \tilde{P} B$. Substituting equation (S18) to the right-hand side of equation (S17), the result follows:

$$\bar{P} = \tilde{Q} - \gamma^2 A^\top \tilde{P} B T(P)^{-1} B^\top \tilde{P} A + \gamma A^\top \tilde{P} A, \tag{S19}$$

which is the variant of the so-called Riccati equation.

Proposition 2 *The Hessian matrix of $G(z_k)$, i.e., $\Delta G(z_k)$, is bounded as*

$$\Delta G(z_k) \le Y(P_k), \tag{S20}$$

where

$$Y(P_k) = \begin{bmatrix} \gamma\frac{1+\epsilon}{\epsilon}L_s + \epsilon\gamma A^\top P_k^2 A & \gamma\epsilon A^\top P_k^2 B \\ \gamma\epsilon B^\top P_k^2 A & \gamma(\frac{1}{\epsilon}+1)L_u + \gamma\epsilon B^\top P_k^2 B \end{bmatrix}.$$

Moreover, if s spans an invariant Koopman subspace for the dynamic model of soft robots, then $G(z) = 0$.

***Proof**. Note that one can rewrite equation (8) as*

$$\begin{aligned} Q(z_k) &= s_{e,k}^\top Q s_{e,k} + s_{e,k}^\top K^\top R K s_{e,k} + \gamma(Fs_{e,k} + w_{e,k})^\top P_k (Fs_{e,k} + w_{e,k}) \\ &\leq s_{e,k}^\top Q s_{e,k} + s_{e,k}^\top K^\top R K s_{e,k} + \gamma s_{e,k}^\top F^\top (P_k + \epsilon P_k^2) F s_{e,k} + \gamma\tfrac{1+\epsilon}{\epsilon} s_{e,k}^\top L s_{e,k}, \end{aligned} \tag{S21}$$

where the last inequality is due to the following fact: Given any constant $\epsilon > 0$, it holds that

$$2 s_{e,k}^\top F^\top P w_{e,k} \leq \epsilon s_{e,k}^\top F^\top P^2 F s_{e,k} + \frac{1}{\epsilon} s_{e,k}^\top L s_{e,k},$$

where $L = L_s + L_u K^\top K$. In view of equation (S21), one has:

$$G(z_k) \leq z_k^\top Y_k z_k,$$

i.e., the condition in equation (S20) holds. Moreover, if s spans an invariant Koopman subspace for the dynamic model for soft robots, the uncertainty in equation (1) holds $w = 0$ and it leads to $\Delta G(z) = 0$. □

To state the following Theorems 1 and 2 in a compact form, let $\bar{P}^*$ and $\bar{K}^*$ be the optimal solution of equation (S17) and denote $\bar{H}_i(\bar{P}_i) = \Xi_i(\bar{P}_i) + Y_i(\bar{P}_i)$, where $\bar{P}_i$ is calculated using a value iteration procedure as follows with $\bar{P}_0 = 0$.

1. Value update:

$$\bar{P}_{i+1} = \tilde{Q} - \gamma^2 A^\top \tilde{P}_i B T(\bar{P}_i)^{-1} B^\top \tilde{P}_i A + \gamma A^\top \tilde{P}_i A. \tag{S22a}$$

2. Policy update:

$$\bar{K}_{i+1} = -\gamma T(\bar{P}_i)^{-1} B^\top \tilde{P}_i A. \tag{S22b}$$

Theorem 1 *Under Assumption 1 and $ZZ^\top$ is full rank, given $\hat{H}_0 = \bar{H}_0(P_0)$ and $K_0 = \bar{K}_0$, the iteration of $\hat{H}_i$, using the least-square update rule (11), satisfies $\hat{H}_i \leq \bar{H}_i(\bar{P}_i)$ for any $i \in \mathbb{N}$. Moreover, $\hat{H}_\infty \leq \bar{H}(\bar{P}^*) := \bar{H}^*$.*

Proof. One first rewrites:

$$\begin{aligned} d(z_{i,k}, \hat{H}_i) &= l(z_{i,k}) + z_{i,k+1}^\top \gamma \hat{H}_i z_{i,k+1} \\ &\leq z_k^\top v \left(\Xi_i(P_{k,i}) + Y_i(P_{k,i})\right), \end{aligned} \tag{S23}$$

where $P_i = \begin{bmatrix} I & K_i^\top \end{bmatrix} \hat{H}_i \begin{bmatrix} I & K_i^\top \end{bmatrix}^\top$. Note that the computation of $\bar{H}_i(\bar{P}_i)$ via the iteration on $\bar{P}_i$ with equation (S22a) is equivalent to the iteration on H_{i+1} under $H_0 = \bar{H}_0(\bar{P}_0)$.

Hence, by using the Kronecker products, from equation (11) and equation (S23), one computes:

$$\begin{aligned} h_{i+1} &\leq (ZZ^\top)^{-1}(ZZ^\top) v \left(\Xi_i(P_{k,i}) + Y_i(P_{k,i})\right) \\ &= v \left(\Xi_i(P_{k,i}) + Y_i(P_{k,i})\right) \\ &\leq v \left(\Xi_i(\bar{P}_i) + Y_i(\bar{P}_i)\right), \end{aligned} \tag{S24}$$

where $\bar{h} = \mathrm{vec}(\bar{H})$, the last equality holds since $\hat{H}_0 = \bar{H}_0$ and $K_0 = \bar{K}_0$.

In view of the last inequality in equation (S24), it holds that:

$$\hat{H}_{i+1} \leq \bar{H}_{i+1}(\bar{P}_{i+1}). \tag{S25}$$

Similar to the proof argument in[50], the convergence property of the value iteration procedure as in equation (S22) can be stated, that is:

i)$\bar{P}_1 \leq \bar{P}_2 \leq \bar{P}^*$;
ii) $\lim_{i\to+\infty} \bar{P}_i = \bar{P}^*$, $\lim_{i\to+\infty} \bar{K}_i = \bar{K}^*$.
Hence, $\hat{H}_\infty \leq \bar{H}_\infty(\bar{P}_\infty) = \hat{H}_\infty(\bar{P}_\infty) + Y_\infty(\bar{P}_\infty) = \bar{H}^*$. □

Remark 3 *Equation (S25) in Theorem 1 shows that the overall cost-to-go with the least-square update rule (11) is smaller than that using the robust value iteration with the procedure (S22). The latter results in a robust LQR as iteration i goes to infinity. Hence, LERL with the least-square update rule (11) outperforms the robust KCID with the procedure (S22).*

Theorem 2 *Let $\bar{s}_{e,k} = \gamma^{k/2} s_{e,k}$, then the control input computed by :*

$$\bar{u}_{e,k} = -(\hat{H}_{uu,\infty})^{-1} \hat{H}_{us,\infty} \bar{s}_{e,k}, \tag{S26}$$

stabilizes $\bar{s}_{e,k}$.

Poof. Consider two Lyapunov functions:

$$\bar{L}(s_{e,k}) = \|s_{e,k}\|^2_{\bar{P}^*}, \tag{S27a}$$

under $\bar{u}_{e,k} = \bar{K}\bar{s}_{e,k}$, and

$$L(s_{e,k}) = \|(s_{e,k}, \bar{u}_{e,k})\|^2_{\hat{H}_\infty}, \tag{S27b}$$

under control equation (S26). We first show the convergence under the Lyapunov function $\bar{L}(s_{e,k})$ with $\bar{u} = \bar{K}\bar{s}_{e,k}$. To this end, one writes:

$$L(s_{e,k+1}) - L(s_{e,k}) = \|s_{e,k+1}\|^2_P - \|s_{e,k}\|^2_P. \tag{S28}$$

Consider $\bar{s}_{e,k} = \gamma^{k/2} s_{e,k}$. In view of equation (1), one can write:

$$\begin{aligned} \bar{s}_{e,k+1} &= \gamma^{1/2}(A\bar{s}_{e,k} + B\bar{u} + \bar{w}_{e,k}) \\ &= \gamma^{1/2}(F\bar{s}_{e,k} + \bar{w}_{e,k}), \end{aligned} \tag{S29}$$

where the second equality is due to the definition $\bar{u}_{e,k} = \bar{K}^*\bar{s}_{e,k}$. Taking equation (S29) into equation (S28) leads to:

$$\begin{aligned} L(\bar{s}_{e,k+1}) - L(\bar{s}_{e,k}) &= \gamma\|F\bar{s}_{e,k} + \bar{w}_{e,k}\|^2_P - \|\bar{s}_{e,k}\|^2_P \\ &\leq \|\bar{s}_{e,k}\|^2_{\gamma(1+\epsilon)/\epsilon L + \gamma F^\top(P+\epsilon P^2)F - P} \\ &= -\|\bar{s}_{e,k}\|^2_{\bar{Q}+K^\top RK} \\ &< 0. \end{aligned} \tag{S30}$$

Hence, the state $\bar{s}_{e,k}$ converges to the origin asymptotically under $\bar{u}_{e,k} = \bar{K}^*\bar{s}_{e,k}$.

In view of the results that $\hat{H}_\infty \leq \bar{H}^*$ and also note that $\bar{L}(s_{e,k}) = \|z_k\|^2_{\bar{H}^*}$, we get:

$$L(s_{e,k}) \leq \bar{L}(s_{e,k}),\ \forall\, k \in \mathbb{N}.$$

□

Remark 4 *Theorem 2 implies that under the control policy in equation (S26), the state $s_{e,k}$ converges to the origin asymptotically when γ is close to 1.*

Supplementary Table 3. Parameters for LERL and KCID

a

Parameter	Lifting dimension	Linear regression loss weight	Reconstruction loss weight	Regularization loss weight	Eigenvalue loss weight	Singular value loss weight	MLP Network Structure	Activation function	Learning rate	Optimizer	Eigenvalue threshold η_1	Singular value threshold η_2
Value	12	10	1	1	0.003	0.003	12-64-128 -64-12	ReLU	0.0003	Adam	0.5	0.2

b

Parameter	Type I robot configuration $\mathbf{E}_{\mathrm{S}}^{1}$			Type I robot configuration $\mathbf{E}_{\mathrm{S}}^{3}$–$\mathbf{E}_{\mathrm{S}}^{4}$–$\mathbf{E}_{\mathrm{L}}^{2}$			Type III robot configuration $\mathbf{E}_{\mathrm{M}}$–$\mathbf{E}_{\mathrm{L}}$	
	Target regulation	Circular tracking	Bow-tie tracking	Target regulation	Circular tracking	Bow-tie tracking	Target regulation	Circular tracking
Q	$\mathrm{diag}\{3\cdot 1_3, 1_{21}, 5\cdot 1_3, 2.5\cdot 1_3\}$	$\mathrm{diag}\{1_{24}, 4\cdot 1_3, 2\cdot 1_3\}$	$\mathrm{diag}\{1_{24}, 4\cdot 1_3, 2\cdot 1_3\}$	$\mathrm{diag}\{1_{24}, 4\cdot 1_3, 2\cdot 1_3\}$	$\mathrm{diag}\{1_{24}, 4\cdot 1_3, 2\cdot 1_3\}$	$\mathrm{diag}\{1_{24}, 4\cdot 1_3, 2\cdot 1_3\}$	$\mathrm{diag}\{1_{24}, 5\cdot 1_3, 0_3\}$	$\mathrm{diag}\{1_3, 0_3, 1_3, 0_3, 1_{12} 5\cdot 1_3, 0_3\}$
R	$\mathrm{diag}\{8\cdot 1_4\}$	$\mathrm{diag}\{5\cdot 1_4\}$	$\mathrm{diag}\{3\cdot 1_4\}$	$\mathrm{diag}\{25\cdot 1_3\}$	$\mathrm{diag}\{8\cdot 1_3\}$	$\mathrm{diag}\{8\cdot 1_3\}$	$\mathrm{diag}\{40\cdot 1_3\}$	$\mathrm{diag}\{40\cdot 1_3\}$
Discount factor	0.98							

c

Parameter	LERL with Gaussian kernel embedding	LERL with time-delay embedding
Embedding	$s = e^{-\gamma\|x-c\|^2},\ c\in[-1,1]$	$s_i = [s_i, s_{i-1}, s_{i-2}]^\top$
Q	$\mathrm{diag}\{5\cdot 1_3, 2\cdot 1_3, 1_{18}\}$	$\mathrm{diag}\{0.06\cdot 1_3, 0.03\cdot 1_9, 0.12\cdot 1_3, 0.03\cdot 1_9\}$
R	$\mathrm{diag}\{25\cdot 1_{12}\}$	$\mathrm{diag}\{5\cdot 1_{12}\}$
Discount factor	0.98	

d

Parameter	Learning rate	Batch size	ϵ_{adam}	$\beta_{1,\mathrm{adam}}$	$\beta_{2,\mathrm{adam}}$
Value	0.0005	50	1e-8	0.9	0.9999

E

Parameter	Q	R
Value	$\mathrm{diag}\{3\cdot 1_3, 1_{21}, 2\cdot 1_3, 1_3\}$	$\mathrm{diag}\{4\cdot 1_4\}$

a, Offline Koopman embedding training parameters. **b,** Online policy learning parameters for Type I and II soft robots in three configurations. **c,** Parameters for LERL with Gaussian kernel and time-delay embeddings. **d,** Adam parameters for online policy update. **e,** Parameters for KCID.
Note that $1_n = [1, \cdots, 1] \in \mathbb{R}^n$.

Supplementary Video 1. Hammering nails task

LERL-enbled elephant-trunk robot strikes nails with a 370 g weighted hammer to bind two wooden boards. At the beginning of the task, the robot was controlled to grip the hammer handed to it by a human. The robot then used the hammer to quickly drive nails into both sides of the wooden board. This video showcases the capabilities of soft robots powered by LERL for daily assistive and industrial applications.

Supplementary Video 2. Serving drinks with safe interactions

This video shows that LERL enables the elephant-trunk robot to complete the drinks-serving task with safe human-robot interactions, emulating a skilled human bartender. The elephant-trunk robot interacts with the human safely through a fist bump and handshake, adaptively adjusts its position and orientation to smoothly pour drinks into the cup, throws the cup into the trash can, and hands the cup to the guest gently and safely. In addition, the robot remains stable during drinks-serving even under external human interventions. This video demonstrates our approach's capability in precise and smooth control under dynamic loads of drinks, highlighting the potential in daily delicate task operations that require safe human-robot interactions.

Supplementary Video 3. Calligraphy brush handwriting

LERL learns from environmental feedback to enable the hybrid soft robot, combined with two honeycomb and one soft-muscle segment, to perform flexible movements, writing characters "L", "E", "R", "L" with fluid and clear strokes, while ensuring stability in each brushstroke. LERL ensures that the brush tip, mounted at the robot's end, accurately and stably hovers at a specific height above the paper while precisely following the character strokes.

Supplementary Video 4. Quick hand-eye reaction game

LERL enables the worm robot to play a quick hand-eye reaction game. A camera detects the movements of sticks to determine which stick falls. Then, the worm robot equipped with a net pocket on its tip moves quickly to catch the free-fall stick within 100 ms. This video demonstrates the potential of our LERL framework for challenging tasks that require high-performing control in high-speed conditions.

Supplementary Video 5. Policy adaptation performance validation

This video first shows that the online learned control policies drive the honeycomb segment E_S^1 to accomplish target reaching, circle tracking, and bow tie tracking tasks. Then, its policy is transferred and further updated online to drive three types of soft robots in diverse configurations to complete circle and bow tie tracking tasks. This video validates the real-time policy adaptation of LERL to soft robots in multiple configurations.

Supplementary Video 6. Empirical robustness validation

This video presents the empirical robustness validation results of elephant-trunk robots. LERL enables elephant-trunk robots to achieve precise full-state tracking even under heavy loads of 200 g, 500 g, and 1 kg, and actuator faults with 22 broken airbags. LERL's resilience to hardware degradation addresses a critical barrier for field applications, where material fatigue or actuator failure is inevitable.

Supplementary Video 7. Performance improvement from online learning

Comparison of control performance before and after learning in elephant-trunk and worm robots. Control performance improves substantially throughout the learning process, validating the online learning capability of LERL.

Supplementary Video 8. Fast-moving traction stick tracking

The elephant-trunk robot quickly and precisely tracks the fast-moving targets generated from a traction stick manipulated by a human, even under external force interference. This video demonstrates LERL's effectiveness in tracking rapidly moving targets.